International Journal of Hydrogen Energy 68 (2024) 705–721

Contents lists available at ScienceDirect

International Journal of Hydrogen Energy

journal homepage: www.elsevier.com/locate/he

Review Article

Overview and evaluation of crossover phenomena and mitigation measures in proton exchange membrane (PEM) electrolysis

Steffen Fahr [a,*], Franziska K. Engel [a], Sebastian Rehfeldt [a], Andreas Peschel [b,c], Harald Klein [a]

[a] Technical University of Munich, TUM School of Engineering and Design, Department of Energy and Process Engineering, Institute of Plant and Process Technology, Boltzmannstr. 15, Garching, 85748, Bavaria, Germany

[b] Forschungszentrum Jülich GmbH, Institut für nachhaltige Wasserstoffwirtschaft (INW-4), Am Brainergy Park 4, Jülich, 52428, NRW, Germany

[c] RWTH Aachen University, Aachener Verfahrenstechnik, Lehrstuhl für Prozess- und Anlagentechnik für chemische Wasserstoffspeicherung, Forckenbeckstr. 51, Aachen, 52074, NRW, Germany

ARTICLE INFO

Keywords:
PEM electrolysis
Hydrogen crossover
Mass transport
Power-to-X
Recombination catalyst
Oxygen crossover

ABSTRACT

Proton exchange membrane (PEM) electrolysis is widely considered an integral part of the energy transition. Thinner membranes can reduce Ohmic losses and increase efficiency. However, hydrogen crossover limits the use of thinner membranes.

For the first time, this review provides a comprehensive overview of both model and experimental works on hydrogen crossover and crossover mitigation. By combining the experimental data and state-of-the-art models, we discuss the recent progress in understanding crossover mechanisms.

The dominant mechanism for hydrogen crossover is the diffusion driven by both the high hydrogen partial pressures at the cathode and supersaturation in the catalyst layer due to transport limitations. The reviewed models successfully reproduce the experimental data obtained by different groups. A variety of strategies for including recombination catalysts in the cell are currently investigated in academic and corporate research. Some of these show promising results with potential for near-term industrial application.

1. Introduction

Water electrolysis is considered an integral part of the energy transition. Moving from fossil fuels and feedstocks to renewable sources of electricity requires converting electricity to chemical energy. Water electrolysis is one of the few technologies enabling this conversion that are mature enough for near-term and profitable employment. Major water electrolysis technologies are alkaline electrolysis (AEL), proton exchange membrane (PEM) electrolysis, solid oxide electrolysis cells (SOEC), and anion exchange membrane (AEM) electrolysis. Among these, AEL is the most matured technology for large-scale applications with the others named in the order of descending technology maturity [1,2].

PEM electrolysis is today considered a commercial technology, even if upscaling to larger plants in the order of 100 MW is still ongoing [1,3]. In the PEM electrolysis cell, liquid water is fed to the anode, where it is split into oxygen and protons. The PEM allows the protons to migrate to the cathode side, where they are reduced to hydrogen [4]. As the PEM is a dense membrane, usually based on perfluorosulfonic acid (PFSA) polymers, the anode and cathode compartment can be operated with different pressures on either side. While today being more costly than AEL [5] and less efficient than SOEC, PEM electrolysis offers the advantages of fast load changes and the ability to operate at low part load [4]. These make the PEM technology suitable for coupling with a highly volatile renewable energy supply or offering grid services [6].

Closely coupling electrolysis plants to renewable energy generation requires operation at low loads as well as complete shutdowns. In large-scale plants, low-load operation can in principle be achieved by shutdown of individual modules and operation of the remaining modules at moderate load. However, operating individual modules at low load has the potential benefit of energy savings due to the characteristic polarization curve of PEM electrolyzers [6].

Unfortunately, low-load operation is associated with an increase in the share of hydrogen and oxygen that diffuses through the membrane and contaminates the respective other gas stream. As the cell's load, or equivalently its current density, is reduced, the amount of gas produced at the electrodes decreases proportionally according to Faraday's law. However, the gas crossover flux is only reduced disproportionately if at all. Therefore, at low load, a similar amount of hydrogen crosses over to the anode side while it is diluted less with oxygen evolved at the anode.

* Corresponding author.
E-mail address: steffen.fahr@tum.de (S. Fahr).

https://doi.org/10.1016/j.ijhydene.2024.04.248
Received 21 February 2024; Received in revised form 12 April 2024; Accepted 21 April 2024
Available online 30 April 2024

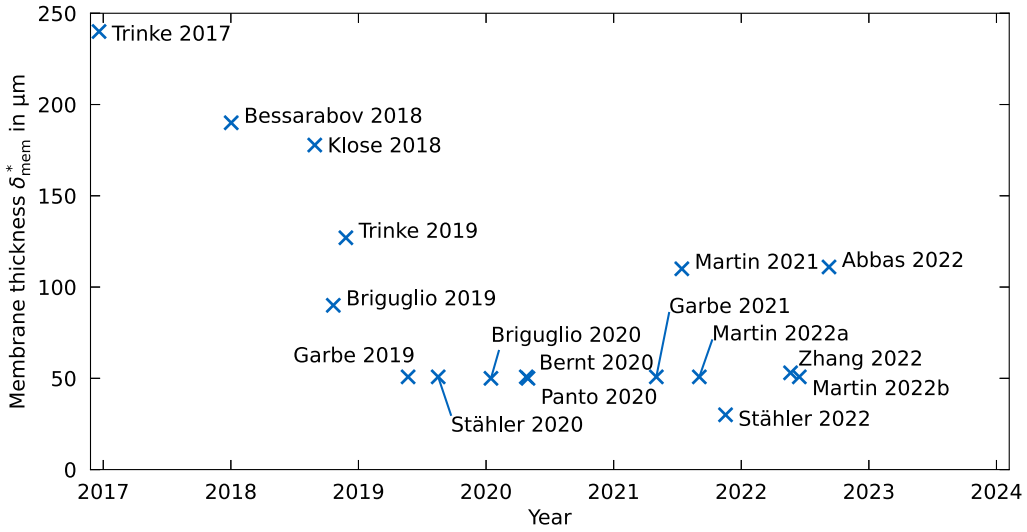

Fig. 1. Experimental works considered in this review plotted by thinnest membrane considered over publication date of the work. Only experimental setups including a fully functional electrochemical cell (no pure permeation experiments) are included. Membrane thickness is given as the thickness specified by the manufacturer, not in fully hydrated condition.

As a result, the electrolyzer must be shut down below a certain load, or otherwise, the lower explosion limit of 4 mol-% hydrogen in oxygen or the commonly used safety limit of 2 mol-% hydrogen in oxygen [7–9] is reached. Oxygen crossover is generally considered less critical due to the smaller crossover flux than hydrogen and the recombination taking place on the cathode as further discussed in Section 5.

In recent years, hydrogen crossover has received an increasing amount of attention. One reason is the general trend towards thinner membranes. The membrane accounts for a significant portion of the overvoltage in PEM electrolysis, especially at high current densities [5,10]. Therefore, reducing its thickness is a major lever in increasing efficiency and reducing operational expenses [5,10]. Fig. 1 shows an overview of the respective thinnest membrane used over the submission date of experimental works on hydrogen crossover considered in this review. In case multi-layer membranes as described in Section 6 were employed, we plotted the reported overall membrane thickness. The data points are unambiguously assigned to their references in Table 1 of the supplementary information (SI). There has been a clear trend in the last five years towards thinner membranes with possible stagnation around 50 µm, e.g., Nafion™ 212 [11], Aquivion® E98-05S [12], and 3M NSTF 50 µm 825 EW membranes [13]. As the diffusion rate is inversely proportional to membrane thickness, crossover increasingly becomes a concern for thinner membranes.

This review addresses both the experimental and the theoretical work in gas crossover in PEM electrolysis. We reproduce mechanistic models from the literature and by applying them to the currently published experimental data evaluate both the data and the mathematical models. Finally, we give a comprehensive overview of recombination catalysts as an enabler of the next generation of PEM electrolysis.

The remainder of this work is structured as follows. In Section 2, we discuss proposed physical mechanisms and modeling approaches for hydrogen crossover. Section 3 deals with the impact of current density on hydrogen crossover comparing observations from different experimental works. In Section 4, we cover the influence of cell compression, cathode ionomer content, and membrane material on hydrogen crossover. Section 5 covers the topic of oxygen crossover, and in Section 6, we present an overview of crossover mitigation measures based on recombination catalysts.

2. Transport mechanisms in PEM electrolysis cells during operation

Multiple transport phenomena are involved in the transport of the four main components, namely protons, hydrogen, oxygen, and water in PEMs under electrolysis operation [14,15]. As PEMs are dense membranes, the dominant transport mechanism of gases inside the membranes is the diffusion driven by concentration gradients, which will be discussed in Section 2.1. The highest chemical potential of the products can be found at their respective production sites, i.e., near the catalyst particles, with decreasing gradients towards the phase boundaries of gas bubbles in the anode and cathode channels. The corresponding concentration peak in the liquid phase is commonly referred to as oversaturation [16] or supersaturation [17] as the concentration is higher than the one expected according to the thermodynamic equilibrium with the gas phase. This supersaturation is made responsible for an increased gas crossover at elevated current density and will be discussed in Section 2.1.

The second notable transport mechanism that has been shown to significantly affect crossover is the convective transport of dissolved gases with the liquid water moving inside the membrane. Movement of the water phase is driven by the pressure difference between cathode and anode as well as electroosmotic drag [14,15]. This mechanism will be covered in the first part of Section 2.2.

In addition to the diffusion term, some works include a term for pressure-driven gas transport through the membrane, sometimes referred to as convection [15,18,19]. However, as the absolute pressure is also indirectly accounted for via its influence on the concentration in the diffusion term, an additional influence is unexpected. Schalenbach et al. [20] confirmed in permeation experiments without any electrical current that the absolute pressure difference has no significant effect on crossover, while the hydrogen partial pressure has the effect that is expected according to Fick's law. There is, however, a possible effect of the pressure difference across the membrane that works via the reduction of water flux from the anode to the cathode [7] as mentioned above. This will be discussed in the second part of Section 2.2.

2.1. Gas diffusion in PFSA membranes

As the interaction between different diffusing species is negligible, diffusion is commonly modeled assuming Fick's law [20]. When modeling gas crossover in electrolysis, this transport mechanism is commonly considered to be the dominant one and others are neglected [17,21]. As Franz et al. [22] visualized in their supplementary information, this leads to linear concentration profiles of gases across the membrane. Fick's law for hydrogen in Nafion™ in one dimension can be written as

$$J^{\mathrm{diff}}_{\mathrm{H_2}} = -D^{\mathrm{eff}}_{\mathrm{H_2}} \cdot \frac{d\, c_{\mathrm{H_2}}}{d\, z}\,, \tag{1}$$

where $J_{H_2}^{diff}$ denotes the hydrogen flux, $D_{H_2}^{eff}$ denotes the effective diffusion coefficient of hydrogen in the membrane, c_{H_2} is the dissolved hydrogen concentration in the liquid phase, and z denotes the spatial dimension into the membrane plane from cathode to anode. An additional index of $D_{H_2}^{eff}$ denoting the material in which the diffusion takes place (the wet PEM in this case) is omitted for better readability. Ito et al. [23] give an overview of the diffusion properties of hydrogen and oxygen in dry Nafion™, pure water, and wet Nafion™ membranes. The compiled data from various literature sources show that the permeability of wet Nafion™ spreads across approximately half an order of magnitude at a given temperature and can be well described by an Arrhenius-type equation [23].

The permeability P_i is defined as the product of the effective diffusion coefficient and the solubility S_i

$$P_i = D_i^{eff} \cdot S_i \tag{2}$$

and measured, e.g., in units of mol cm^{-1} s^{-1} Pa^{-1} [23]. As for modeling PEM electrolysis cells, it is often necessary to separate the phenomena of solution and diffusion, many works use separate formulas for calculating the diffusion coefficient and the solubility of oxygen and hydrogen in wet ionomer membranes. Wise and Houghton [24] developed a correlation for the diffusion coefficients that reads

$$D_i = D_{i0} \cdot \exp\left(\frac{-E_{Ai}}{\bar{R} \cdot T}\right), \tag{3}$$

where D_i is the diffusion coefficient of $i = H_2, O_2$ in water and D_{i0} denotes the pre-exponential factor of the Arrhenius equation. T denotes the temperature, E_{Ai} the activation energy and $\bar{R}$ the ideal gas constant [17,23,24]. The corresponding material parameters are given in Table 1 [23,24].

The effective diffusion coefficient in wet Nafion™ membranes D_i^{eff} can be calculated from the diffusion coefficient in water D_i by multiplication with the water volume fraction ε and division by the tortuosity τ, [17]

$$D_i^{eff} = D_i \cdot \frac{\varepsilon}{\tau}. \tag{4}$$

Both ε and τ are specific to membrane material. Especially on τ, there is only limited information available in the literature. Often, it is avoided by using the Bruggeman correlation [25],

$$D_i^{eff} = D_i \cdot \varepsilon^q, \tag{5}$$

where the exponent q is typically assumed to be 1.5 [22,25]. Alternatively, a value of $\tau = 1.5$ is sometimes assumed [26,27], which is roughly equivalent to using the Bruggeman correlation for a water volume fraction of $\varepsilon = 42\%$. We will discuss the accuracy of this assumption based on measurements from the literature later in this review.

The water volume fraction can be calculated for a known equivalent weight (EW) and water uptake λ to be

$$\varepsilon = \frac{\lambda \cdot \bar{V}_{H_2O}}{\bar{V}_{mem} + \lambda \cdot \bar{V}_{H_2O}}, \tag{6}$$

where λ is defined as the moles of water divided by the moles of sulfonic acid sites [28]. $\bar{V}_{H_2O}$ denotes the molar volume of water and $\bar{V}_{mem}$ the volume of the dry membrane per mole of active sites. These parameters can be calculated, respectively, as

$$\bar{V}_{H_2O} = \frac{\bar{M}_{H_2O}}{\varrho_{H_2O}}, \tag{7}$$

$$\bar{V}_{mem} = \frac{EW}{\varrho_{mem}}. \tag{8}$$

Therein, $\bar{M}_{H_2O} = 18.015 \frac{kg}{kmol}$ denotes the molar mass of water and $\varrho_{H_2O} \approx 1000$ kg m^{-3} the density of water at the operating conditions. Most modern Nafion™ membranes, as used for PEM electrolysis, have an EW of 1100 g mol$_{eq}^{-1}$ [29], a density of approximately 2000 kg m^{-3} [28] and a water uptake of 21–22 [29]. With these values, a water volume fraction ε of 41–42% can be calculated according to Eqs. (6)–(8).

Table 1
Diffusion and solubility parameters of hydrogen and oxygen in water used in Eqs. (3) and (12), respectively.

	Hydrogen	Oxygen	Unit	Source
Pre-exponential factor D_{i0}	4.9	4.2	cm^2 s^{-1}	[23]
Activation energy E_{Ai}	16.51	18.38	kJ mol^{-1}	[23]
Solubility coeff. A	−48.1611	−66.73538	–	[31]/[32]
Solubility coeff. B	5528.45	8747.547	K	[31]/[32]
Solubility coeff. C	16.8893	24.45264	–	[31]/[32]

For calculating the permeation of hydrogen to the anode, the concentration of hydrogen at the anode is oftentimes assumed to be zero [21]. For this case and in the absence of other transport mechanisms, Fick's law for hydrogen permeating from the cathode catalyst layer (CL) to the anode CL simplifies to [21,30]

$$J_{H_2}^{diff} = D_{H_2}^{eff} \cdot \frac{c_{H_2}^{cathode\ CL} - c_{H_2}^{anode\ CL}}{\delta_{mem}} \approx D_{H_2}^{eff} \cdot \frac{c_{H_2}^{cathode\ CL}}{\delta_{mem}}. \tag{9}$$

Therein, δ_{mem} denotes the thickness of the wet membrane during operation. This value is typically 10–30% [29] greater than the specification made by the manufacturer, which is usually given for nominal (nearly dry) conditions and referred to as δ_{mem}^* in the following. Note that the concentrations to be used with the effective diffusion coefficient are those in the water phase of the membrane.

Supersaturation. As mentioned above, the product gases evolve at the active sites of the respective catalyst particles and are from there transported to the gas bubbles in the porous transport layers (PTLs). This means that the concentration of hydrogen in the liquid phase is the highest inside the cathode CL and decreases towards both PTLs. This phenomenon was first hypothesized by Oberlin et al. [16], who measured an increased hydrogen crossover flux at increased current density and inferred an oversaturation equivalent on the order of 20 bar. Similarly, oxygen evolves at the anode and its concentration decreases from there in both directions. The phenomena described in the following are all believed to happen analogously for oxygen [33], but are only discussed for hydrogen for conciseness.

The mass transfer from the active site in the CL to the gas phase in the PTL includes encompasses multiple mechanisms such as mass transport of dissolved gas in the liquid phase, transfer to the gas phase and further transport in the gas phase, as well as transport of bubbles through the liquid phase. Due to the plurality of mechanisms likely involved, this phenomenon is usually not modeled assuming Fick's law, but assuming a simple transfer coefficient $k_{H_2}^{cathode}$ [17]. We refer to the according hydrogen flux as

$$J_{H_2}^{transf\ cathode} = k_{H_2}^{cathode} \cdot \left(c_{H_2}^{cathode\ CL} - c_{H_2}^{cathode\ sat}\right). \tag{10}$$

The variable $c_{H_2}^{cathode\ sat}$ describes the (theoretical) concentration of hydrogen in a liquid phase that is in equilibrium with the "bulk" gas phase at the cathode side. As this concentration in the liquid phase may or may not actually exist in the cell, the transport term Eq. (10) describes the spatial transport of dissolved gas to the first gas bubbles, transport of these bubbles to the flow fields, and possible transport resistances of the phase change. The saturation concentration $c_{H_2}^{cathode\ sat}$ can be calculated using the solubility S_{H_2} of hydrogen in water and the hydrogen partial pressure $p_{H_2}^{cathode}$:

$$c_{H_2}^{cathode\ sat} = S_{H_2} \cdot p_{H_2}^{cathode}. \tag{11}$$

The correlations for the solubility of hydrogen in water from Young [31] and oxygen in water from Battino [32] are commonly used in

this context [17,23]. Various alternative expressions for the Henry coefficient, dissolved hydrogen molar fraction at 1 atm, and other measures of hydrogen solubility in water have been fitted throughout the years. Bessarabov and Millet [14] provide a comprehensive overview of published correlations and exemplary numerical values. The original formulas from Young [31] and Battino [32] directly yield the molar fraction of hydrogen and oxygen, respectively, in water at atmospheric pressure. They can be converted to a formula that yields the solubility of gas as a function of temperature by multiplying with the molar volume of water and dividing by the atmospheric pressure [34]. The final formula reads

$$S_i = 0.55\ \frac{\text{mol}}{\text{m}^3\ \text{Pa}} \cdot \exp\left(A_i + \frac{B_i}{T} + C_i \cdot \ln\left(\frac{T}{100\,\text{K}}\right)\right) . \tag{12}$$

The coefficients A_i, B_i, and C_i for $i = \text{H}_2$, O_2 are given in Table 1.

Assuming a constant hydrogen partial pressure $p_{\text{H}_2}^{\text{cathode}}$, solubility S_{H_2} and transfer coefficient $k_{\text{H}_2}^{\text{cathode}}$, a linear relationship between the hydrogen concentration at the active sites $c_{\text{H}_2}^{\text{cathode CL}}$ and the hydrogen flux to the cathode $J_{\text{H}_2}^{\text{Conv cathode}}$ can be derived:

$$c_{\text{H}_2}^{\text{cathode CL}} = \frac{J_{\text{H}_2}^{\text{transf cathode}}}{k_{\text{H}_2}^{\text{cathode}}} + S_{\text{H}_2} \cdot p_{\text{H}_2}^{\text{cathode}} . \tag{13}$$

When additionally assuming that the flux of hydrogen to the anode (crossover) is small compared to that of hydrogen to the cathode, i.e.,

$$J_{\text{H}_2}^{\text{transf cathode}} = \frac{i}{2F} - J_{\text{H}_2}^{\text{cross}} \approx \frac{i}{2F} , \tag{14}$$

and that the transfer coefficient $k_{\text{H}_2}^{\text{cathode}}$ is independent of the current density i, this yields a linear relationship between the current density and the concentration $c_{\text{H}_2}^{\text{cathode CL}}$.

The increase in supersaturation with current density, in turn, leads to an increase in crossover flux according to Eq. (9). Various groups have measured this effect [7,17,35,36]. Trinke et al. [17] discussed a local temperature increase due to heat transport limitations and a local pressure increase due to mass transport limitations in the PTL as alternative explanations for the increase in crossover flux with current density. The authors concluded that only supersaturation can explain an increase in crossover flux at the measured order of magnitude.

Franz et al. [22] created a dynamic model of a PEM electrolysis cell. Using a slightly different approach than suggested here, they modeled the mass transport of hydrogen from the liquid phase to the gas phase by a volumetric mass transfer coefficient k_{H_2} defined as the ratio of volume-specific flux of hydrogen from the liquid phase to the gas phase and the supersaturation $c_{\text{H}_2}^{\text{cathode CL}} - c_{\text{H}_2}^{\text{cathode sat}}$. With this, they were able to reproduce the steady-state crossover measurements from various groups (e.g., [7,30,35–37]) by varying transfer coefficient across approximately one order of magnitude. They further found that the hydrogen concentration in oxygen temporarily peaks for load step-downs, possibly violating the safety limit.

2.2. Convective transport

In addition to the diffusion of hydrogen driven by the gradient in chemical potential, there is some convective transport with the water permeating through the membrane. On the one hand, for differential pressure operation of the cell, the pressure gradient drives water from the cathode side to the anode side [7,14]. On the other hand, electroosmotic drag manifests itself in an approximately constant number of water molecules dragged along with each proton migrating from the anode to the cathode [7,14,23]. Hence, there are two mechanisms working in opposite directions. In practice, the net water flux is always from anode to cathode, i.e., the electroosmotic effect dominates over the pressure effect. Therefore, it is possible to supply water only to the anode without risking the membrane drying out. Anode-only water supply is common practice in today's PEM electrolyzers. The water flux carries dissolved gases with it, which we refer to as convective transport of the gases.

Table 2
Literature values of drag coefficient n_{drag}.

Source	Membrane	Drag coef. n_{drag}	
		At 30 °C	At 80 °C
Onda et al. [39] (correlation)	N117	4.09	4.76
Suermann et al. [38], (correlation)	N117	2.52	3.43
Friedrichs-Schucht et al. [42]	N115	2.2[a]	3.1
Zawodzinski et al. [43]	N117	2.5–2.9	
Medina and Santarelli [40]	Unknown	1.77[a]	2.20[a]
Luo et al. [44]	N117	2.16	3.21

[a] n_{drag} values extrapolated by temperature in this work.

Electroosmotic water drag. Assuming the molar concentration of hydrogen to be much smaller than the molar concentration of water $c_{\text{H}_2} \ll c_{\text{H}_2\text{O}}$, the hydrogen flux caused by dissolved hydrogen that is transported from anode to cathode along with the drag water can be calculated as

$$J_{\text{H}_2}^{\text{drag}} = v_{\text{H}_2\text{O}} \cdot c_{\text{H}_2} , \tag{15}$$

where $v_{\text{H}_2\text{O}}$ is the velocity of the water [7]. According to Martin et al. [35], the convective hydrogen flux can be calculated as

$$J_{\text{H}_2}^{\text{drag}} = \frac{n_{\text{drag}} \cdot i}{F \cdot c_{\text{H}_2\text{O}}} \cdot c_{\text{H}_2} , \tag{16}$$

where F denotes the Faraday constant and n_{drag} the drag coefficient, i.e., the average number of water molecules pulled along with each proton. These equations are consistent, as the velocity of the permeating water is

$$v_{\text{H}_2\text{O}} = \frac{n_{\text{drag}} \cdot i}{F \cdot c_{\text{H}_2\text{O}}} . \tag{17}$$

Like for hydrogen (see Section 2.1), the concentration of water $c_{\text{H}_2\text{O}}$ is that in the water phase (not the membrane overall) and is therefore equal to the molar density of water, i.e., the reciprocal of the molar volume of water given in Eq. (7). The drag coefficient is a temperature-dependent property of the membrane material. Suermann et al. [38] give the following correlation based on their measurements of a Nafion™ 117 membrane in the temperature range of 30–70 °C:

$$n_{\text{drag}} = 0.0182\ \text{K}^{-1} \cdot T - 3 \tag{18}$$

Onda et al. [39] give the correlation

$$n_{\text{drag}} = 0.0134\ \text{K}^{-1} \cdot T + 0.03 \tag{19}$$

based on their own measurements of a Nafion™ 117 membrane. In both equations, T denotes the temperature in K. Their correlation results in significantly greater drag coefficients than the more recently developed correlation by Suermann et al. [38].

Table 2 gives an overview of some experimentally obtained drag coefficients from the literature. We linearly extrapolated the values of the global water drag coefficient (n_g in the work) from Medina and Santarelli [40] at $i = 1\ \text{A cm}^{-2}$ and $p^{\text{cathode}} = 7\,\text{bar}$ to obtain the corresponding values at $T = 30\,°\text{C}$ and 80 °C for better comparison with the remaining works. Hancke et al. [41] measured drag coefficients of 3.7 and 4.2 at 1.5 and 1.86 A cm^{-2}, respectively, for a cathode pressure of 30 bar cathode pressure and a temperature of 50 °C. Overall, the correlation by Suermann et al. [38] appears to represent the data obtained by the different groups better than that by Onda et al. [39].

For their own experimental system at $i = 5\ \text{A cm}^{-2}$, Martin et al. [35] estimated a hydrogen flux due to electroosmotic drag of $J_{\text{H}_2}^{\text{drag}} = 0.26\ \text{mmol m}^{-2}\ \text{s}^{-1}$, which corresponds to approximately 10–20% of the crossover measured at this condition. Since the estimate was based on a relatively low crossover flux corresponding to a low supersaturation, it can be considered rather conservative. Hence, it may be necessary to include the electroosmotic drag term in the crossover calculation in addition to the diffusion term when considering high current densities. Unfortunately, this yields a less straightforward solution than the linear concentration profile obtained when only assuming Fick diffusion.

Pressure-driven water transport. As the cathode pressure typically exceeds the anode pressure in PEM electrolysis, pressure-driven water transport works against the electroosmotic water drag, thereby reducing the velocity of water permeating towards the cathode, v_{H_2O}. Kalinnikov et al. [45] developed a two-phase transport model for modeling the flow of water in liquid and vapor form throughout the different layers of the electrolysis cell. Water transport has important implications for the operating conditions during which the cell remains sufficiently wet for safe operation. However, as water transport itself is not a focus of this work, we only discuss the aspects most relevant for gas crossover.

The pressure-driven transport of water through the membrane has been brought up as a possible influence of differential pressure on gas crossover [7,9,14]. However, it has been argued in previous works that this effect is negligible compared to electroosmotic transport in practical application [7,38].

For instance, Bernt et al. [7] argued that the according transport term would lead to a quadratic dependency of hydrogen crossover on cathode pressure, which is not observed in practice. Increased cathode pressure both increases the hydrogen concentration in the water phase c_{H_2} and reduces the water permeation velocity v_{H_2O} approximately linearly, leading to an overall quadratic dependency in Eq. (15).

Trinke et al. [46] directly investigated the effect of the differential pressure on hydrogen crossover. They measured the crossover flux over the current density for a cathode pressure of 10 bar and varied the anode pressure between 1 bar an 10 bar. No significant influence of differential pressure on hydrogen crossover flux was found for current densities up to 1 A cm^{-2}.

This suggests that the effect of differential pressure on hydrogen crossover is too small to be measured, at least at these conditions. The mechanism can nonetheless be investigated by quantifying the differential pressure effect on water drag, which in turn affects the crossover via the mechanism discussed in Section 2.2.

The differential pressure $\Delta p = p^{\text{cathode}} - p^{\text{anode}}$ can be viewed as a factor influencing the overall drag coefficient n_{drag}, or pressure-driven water transport can be viewed as an entirely separate process with an according permeability coefficient k_{perm}. The connection between these approaches can be written as

$$J_{H_2O}^{\text{drag}} = n_{\text{drag}} \cdot i = n_{\text{drag}}^{*} \cdot i - k_{\text{perm}} \cdot \Delta p \,, \tag{20}$$

where n_{drag}^{*} is the pressure-independent drag coefficient, analogue to the drag coefficient n_{eo} as defined in [40].

The permeability coefficient k_{perm} of a given membrane can accordingly be obtained by measuring electroosmotic drag and varying the differential pressure Δp while keeping temperature and current density constant. Suermann et al. [38], Hancke et al. [41] and Medina and Santarelli [40] performed suitable measurements by varying the cathode pressure while keeping the anode pressure constant. The permeability coefficient can be calculated according to Eq. (22):

$$n_{\text{drag}}^{*} \cdot i = n_{\text{drag}}(\Delta p_1) \cdot i + k_{\text{perm}} \cdot \Delta p_1 = n_{\text{drag}}(\Delta p_2) \cdot i + k_{\text{perm}} \cdot \Delta p_2 \tag{21}$$

$$\Rightarrow k_{\text{perm}} = \frac{\left(n_{\text{drag}}(\Delta p_2) - n_{\text{drag}}(\Delta p_1)\right) \cdot i}{\Delta p_1 - \Delta p_2} \tag{22}$$

Therein, Δp_1 and Δp_2 are the differential pressures over the membrane present during the to measurements.

Suermann et al. [38] measured water drag in an electrolysis cell under operation at differential pressures of 0 and 10 bar. Although the difference in overall drag coefficient was small compared to other influences on the drag coefficient, the two measurements can be taken to estimate the permeability coefficient based on Eq. (22).

Medina and Santarelli [40] report eight measured values of the drag coefficient n_{drag} varying differential pressure between 7 and 70 bar, current density between 0.25 and 1 A cm^{-2} and temperature between 40 and 55 °C. These measurement values allowed us to calculate four values of k_{perm} using Eq. (22).

Table 3
Permeability coefficients calculated from literature values of pressure-driven water permeation.

	δ_{mem}^{*} µm	T °C	i A cm^{-2}	k_{perm} mmol m^{-2} s^{-1} bar^{-1}
Suermann et al. [38]	178	50	2.00	0.655
Medina and Santarelli [40]	254	40	0.25	0.617
Medina and Santarelli [40]	254	40	1.00	0.642
Medina and Santarelli [40]	254	55	0.25	0.712
Medina and Santarelli [40]	254	55	1.00	0.905
Hancke et al. [41]	Unknown	50	1.50	2.641
Hancke et al. [41]	Unknown	50	1.86	3.193
Evans et al. [47] (low)	178	[a]	0	0.305
Evans et al. [47] (high)	178	[a]	0	0.994

[a] Room temperature.

Recently, Hancke et al. [41] published measurements of, among others, the water drag in a 12 kW Nel stack operated at cathode pressures between 5 and 150 bar. Water drag measurements are available at 1.5 and 1.86 A cm^{-2}, respectively at a temperature of 50 °C. The corresponding values of k_{perm} obtained by using Eq. (22) for the data points at 5 and 150 bar can also be found in Table 3 along with those based on [38,40].

Evans et al. [47] directly investigated the permeation of liquid water in Nafion™ 117 membranes under differential pressure and without electrolysis operation. They obtained permeabilities of 5.5–17.9 · 10^{-14} m Pa^{-1} s^{-1} (m^3 s^{-1} of volume flow per m^2 of area and Pa of differential pressure) for untreated membranes. Assuming a density of water of $\rho_{H_2O} \approx 1000$ kg m^{-3}, these can be converted to 0.305–0.994 mmol m^{-2} s^{-1}, which we added to Table 2 for comparison.

Overall, the permeability coefficients reported in Table 2 based on the literature agree well with one another with the exception of those calculated based on the results from [41], which imply a five-fold higher effect of differential pressure on water transport. Certainly, the membrane thickness plays into the value of k_{perm} with presumably an inversely proportional relationship between k_{perm} and δ_{mem}. Unfortunately, the membrane thickness in Nel prototype stack investigated by Hancke et al. [41] is not reported.

While some works point towards negligible influence of the differential pressure on hydrogen and water transport [38,46,47], Medina and Santarelli [40] and Hancke et al. [41] showed a strong relationship between differential pressure and water drag. This apparent disagreement is in part due to the different operating conditions. Medina and Santarelli [40] work at more than six times higher differential pressures while operating in part at eight times lower current density compared to Suermann et al. [38]. When taking this into account, these works agree well on the magnitude of the permeation coefficient. Still, additional work on this topic would be desirable, especially considering to the disagreement between Medina and Santarelli [40] and Hancke et al. [41] despite the relatively similar study design based on 5 and 12 kW high-pressure PEMEL stacks.

2.3. Overall transport

Based on Sections 2.1 and 2.2, we suggest modeling crossover by either only considering the diffusion mechanism or diffusion and electroosmotic drag. Pressure-driven water transport represents at most a fraction of electroosmotic transport (if it exceeded electroosmotic transport, the cathode side of the membrane would dry out), which itself only has a moderate effect on hydrogen crossover at practical current densities [35]. Pressure-driven water transport can in principle be considered by using a pressure-dependent drag coefficient. However, we do not recommend this, as results in a current-density-dependent drag coefficient according to Eq. (20).

Neglecting pressure-driven water transport and assuming no gas transport driven by the absolute pressure difference (Darcy law), the

total hydrogen flux from the cathode CL to the anode at the depth z in the membrane can be described by the equation

$$\begin{aligned} J_{H_2}^{cross}(z) = J_{H_2}^{cross} &= J_{H_2}^{diff}(z) - J_{H_2}^{drag}(z) \\ &= -D_{H_2}^{eff} \cdot \frac{d\, c_{H_2}(z)}{d\, z} - \frac{n_{drag} \cdot i}{F \cdot c_{H_2O}} \cdot c_{H_2}(z) \\ &= -D_{H_2}^{eff} \cdot \frac{d\, c_{H_2}(z)}{d\, z} - v_{H_2O} \cdot c_{H_2}(z)\ . \end{aligned} \tag{23}$$

Drawing a steady-state mass balance around a membrane element and assuming only transport perpendicular to the membrane surface yields the second order homogeneous differential equation

$$\begin{aligned} \frac{d J_{H_2}^{cross}}{d\, z} = 0 &= -\frac{d}{d\, z}\left(D_{H_2}^{eff} \cdot \frac{d\, c_{H_2}(z)}{d\, z} \right) - \frac{d}{d\, z}\left(v_{H_2O} \cdot c_{H_2}(z) \right) \\ &= -D_{H_2}^{eff} \cdot \frac{d^2\, c_{H_2}(z)}{(d\, z)^2} - v_{H_2O} \cdot \frac{d\, c_{H_2}(z)}{d\, z}\ . \end{aligned} \tag{24}$$

This is the steady-state version of the equation derived by Franz et al. [22]. The analytical solution of this differential equation is

$$c_{H_2}(z) = A \cdot e^{-\left(\frac{v_{H_2O}}{D_{H_2}^{eff}}\right) \cdot z} + B \tag{25}$$

with the parameters A and B to be adjusted to the boundary conditions. These conditions can, for example, be

$$J_{H_2}^{cross}(z = \delta_{mem}) = J_{H_2}^{cross} = J_{H_2\ measured}^{cross}\ , \tag{26}$$

$$c_{H_2}(z = \delta_{mem}) = 0\ . \tag{27}$$

By combining Eqs. (25), (23), (26) and (27), we obtain the expression

$$J_{H_2}^{cross} = D_{H_2}^{eff} \cdot A \cdot \frac{v_{H_2O}}{D_{H_2}^{eff}} \cdot e^{-\left(\frac{v_{H_2O}}{D_{H_2}^{eff}}\right) \cdot \delta_{mem}} \tag{28}$$

$$\Leftrightarrow A = \frac{J_{H_2}^{cross}}{v_{H_2O}} \cdot e^{\left(\frac{v_{H_2O}}{D_{H_2}^{eff}}\right) \cdot \delta_{mem}}\ . \tag{29}$$

This allows us to calculate the constant A. Subsequently, the constant B can be determined as

$$\begin{aligned} B &= c_{H_2}(\delta_{mem}) - A \cdot e^{-\left(\frac{v_{H_2O}}{D_{H_2}^{eff}}\right) \cdot \delta_{mem}} \\ &\approx -A \cdot e^{-\left(\frac{v_{H_2O}}{D_{H_2}^{eff}}\right) \cdot \delta_{mem}} = -\frac{J_{H_2}^{cross}}{v_{H_2O}}\ . \end{aligned} \tag{30}$$

Overall, we obtain the concentration profile

$$c_{H_2}(z) = \frac{J_{H_2}^{cross}}{v_{H_2O}} \cdot \left(e^{\left(\frac{v_{H_2O}}{D_{H_2}^{eff}}\right) \cdot (\delta_{mem} - z)} - 1 \right)\ , \tag{31}$$

where the coordinate z is zero at the cathode catalyst site. For comparison, the more trivial linear profile resulting from only Fick diffusion can be described by

$$c_{H_2}(z) = \frac{J_{H_2}^{cross}}{D_{H_2}^{eff}} \cdot (\delta_{mem} - z)\ . \tag{32}$$

We plotted the resulting concentration profiles of Eqs. (31) and (32) in Fig. 2 exemplarily for three current densities and the corresponding crossover flux measured by Martin et al. [35]. We used Eqs. (3) and (4) to calculate the diffusion coefficient $D_{H_2}^{eff}$ assuming a tortuosity and water volume fraction of $\tau = 1.5$ and $\varepsilon = 0.42$, respectively. Eqs. (17) and (18) were used to calculate the water velocity v_{H_2O} assuming a water concentration of $c_{H_2O} = 0.054\ mol\ cm^{-3}$ [35]. The hydrogen saturation concentration was calculated using Eqs. (12) and (11) after subtracting the water vapor pressure from the total cathode pressure to obtain the hydrogen partial pressure. The wet membrane thickness of 63 µm was adopted from Martin et al. [35].

The concentration profiles in the left part of the plot (hatched area, PTL and CL) of Fig. 2 are only included for easier reading and are not meant to represent the true shape of the profile in this region. As the exact transport mechanism is unknown and possibly a mix of different mechanisms, the exact profile is unknown and likely not linear. By using a volumetric mass transfer coefficient and spatially discretizing the cathode CL, Franz et al. [22] obtained a more realistic concentration curve of dissolved hydrogen in the CL.

The plot (Fig. 2) confirms that the effect of water drag on hydrogen crossover is only notable at high current densities. For high current densities and with the chosen boundary conditions Eqs. (26) and (27), the nonlinear model including the drag mechanism predicts a significantly higher supersaturation than the linear model based on diffusion only. The figure further shows how the supersaturation approaches zero at small current densities. Nonetheless, supersaturation must be taken into account even for moderate current densities.

3. Current density effect on hydrogen crossover

As visualized in Fig. 2, increased current density raises the hydrogen concentration at the reaction site $c_{H_2}^{cathode\ CL}$ according to Eq. (13) and thereby increases the hydrogen crossover. The relationship between current density and supersaturation is approximately linear in case the transfer coefficient $k_{H_2}^{cathode}$ is independent of the current density.

A variety of measurements of this effect have been published in the literature. We compiled a comprehensive selection of experimental data from various groups in Fig. 3. We identified membrane thickness, temperature, and cathode pressure as the most important experimental influences. We found that normalizing the measured crossover flux by the membrane thickness makes data from different experiments more comparable. Therefore, we normalized all data to a membrane thickness of $\delta_{mem}^{*} = 50.8\,\mu m$ (Nafion™ 212), referring to the manufacturer's specifications rather than the actual wet membrane thickness. Normalization was achieved by multiplication with the membrane thickness used (manufacturer's specification) and division by 50.8 µm. Note that this normalization is exact when exclusively considering diffusion-driven transport according to Eq. (9). Electroosmotic drag is independent of the membrane thickness, which, in theory, leads to disproportionately lower crossover in thicker membranes, especially at high current densities. Nonetheless, we decided the simple scaling was sufficient for the visual comparison given in Fig. 3. Another version of the figure that allows to assign the individual curves to the publication they are adopted from is given in the supplementary information.

The figure focuses on works that vary the pressure and use Nafion™ brand membranes or ionomer. Garbe et al. [8,48], Martin et al. [49], and Klose et al. [11] examined recombination catalysts in the membrane, which will be discussed in Section 6. In Fig. 3, we only included the reference measurements without recombination catalyst. Martin et al. [37] measured crossover at varying cell compression levels, which will be discussed in Section 4.1. Here, we only include the data at the lowest compression level.

While the crossover flux measured by different groups at identical temperature, cathode pressure, and current density can vary quite widely at high current densities, the curves for given cathode pressure and temperature tend to converge towards the same crossover flux at near-zero current density. This is in line with the model equations presented in Section 2, as towards zero current density, only the diffusion driven by $p_{H_2}^{cathode}$ prevails, which should be the same for the considered works all using Nafion™ membranes.

To visualize this, we extrapolated all data shown in Fig. 3 to zero current density (shown in Fig. 4). As not all graphs appear linear in Fig. 3, we chose the following heuristic to determine the theoretical

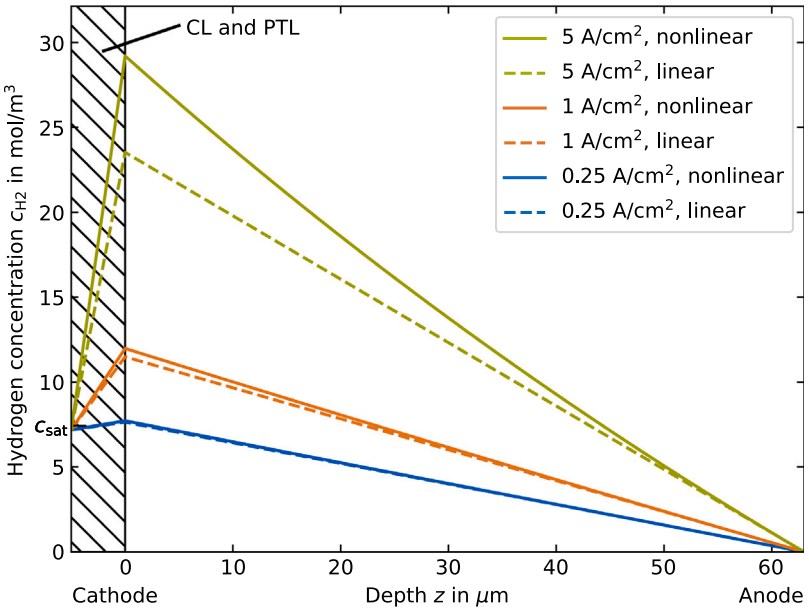

Fig. 2. Modeled hydrogen concentration profiles inside Nafion™ 212 membrane at 80 °C and 10 bar according to Eq. (31) (nonlinear) and Eq. (32) (linear). *Source:* Data on crossover flux was adopted from Martin et al. [35].

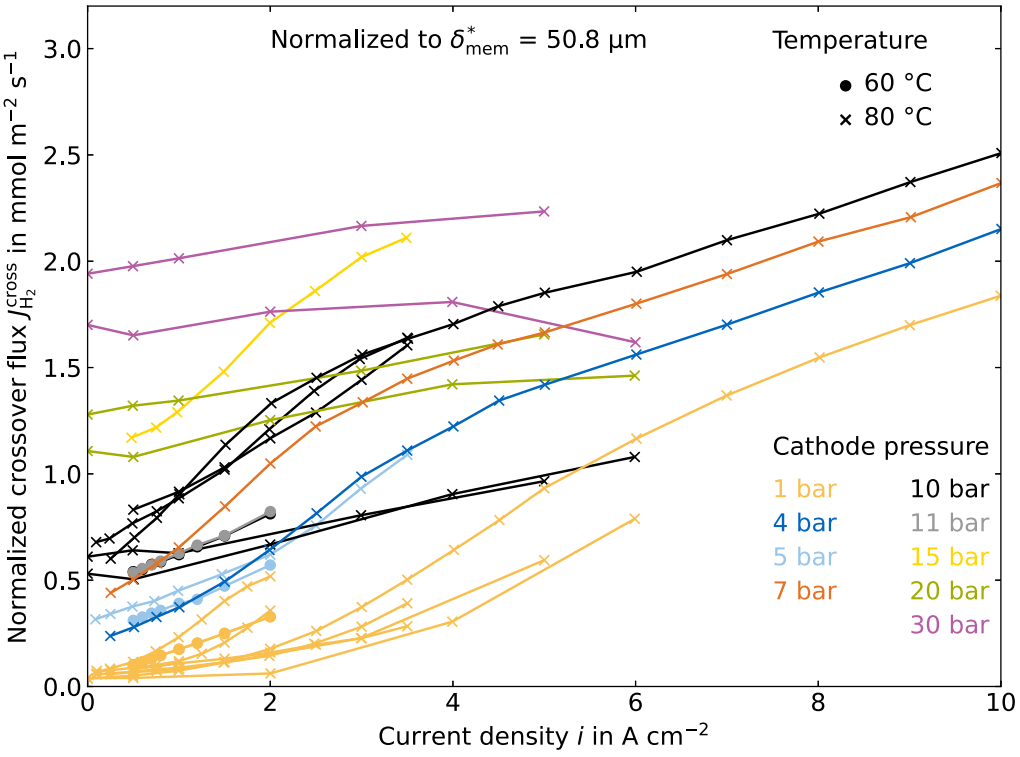

Fig. 3. Visualization of crossover fluxes reported in the literature at different temperature, cathode pressure and current density. Data was adopted from [7,8,11,35,37,48,49] and linearly normalized by the membrane thickness δ^*_{mem}. For an allocation of all curves to the references, see SI.

crossover at zero current density: We obtained the average slope s_{avg} of the curves by linear interpolation between 0 and 4 A cm^{-2}. Then, we estimated the crossover flux at zero current density by extrapolation from the data point with the lowest current density, $(i_{min}, J^{diff}_{H_2\,min})$ according to Eq. (33).

$$J^{diff}_{H_2\,0} = J^{diff}_{H_2\,min} - s_{avg} \cdot i_{min} \,. \tag{33}$$

Subsequently, we plotted the obtained theoretical crossover at zero current density over the hydrogen partial pressure determined as the difference of the cathode pressure and the water vapor pressure at the given temperature (Fig. 4). All data was measured at a temperature of either 60 or 80 °C, as indicated by the color of the data points.

Although the crossover data at a temperature of 60 °C is relatively sparse, a linear fit of the crossover at zero current density over the pressure coincides remarkably well with the presented model for both temperatures. We calculated the diffusion coefficient and solubility using Eqs. (3) and (12), respectively, and assumed a tortuosity of τ = 1.5 and a water volume fraction of ε = 0.42.

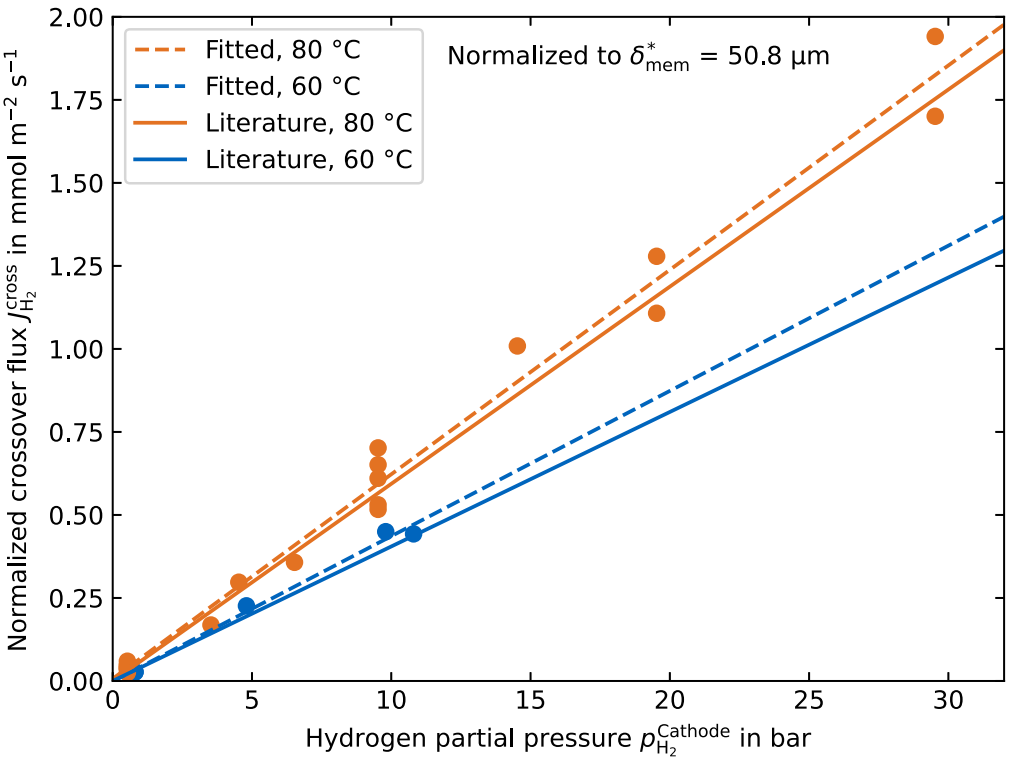

Fig. 4. Extrapolated theoretical crossover flux at zero current density over cathode hydrogen partial pressure $p^{cathode}_{H_2}$. Data was adopted from [7,8,11,35,37,48,49] and linearly normalized by the membrane thickness δ^*_{mem}. (For interpretation of the references to color in this figure legend, the reader is referred to the web version of this article.)

The mass transfer coefficient $k^{cathode}_{H_2}$ for the transport of hydrogen from the cathode CL to the cathode gas phase can be determined by Eq. (13) when measured crossover data is available. The cathode CL hydrogen concentration $c^{cathode\ CL}_{H_2}$ can be determined by using $z = 0$ in Eq. (31) or Eq. (32). The resulting values of the transfer coefficient $k^{cathode}_{H_2}$ for the data measured by Martin et al. [37] and Garbe et al. [48] are exemplarily shown in Fig. 5. The dashed lines represent the linear transport model without electroosmotic drag and the solid lines the model with electroosmotic drag. The transfer coefficients appear to be relatively constant around a value of 0.01 m s^{-1} for current densities larger than 1 A cm^{-1} with the exception of the 1 bar graph for [37]. Below 1 A cm^{-1}, the calculated $k^{cathode}_{H_2}$ values decline. This could mean that the actual transfer coefficients decline, or, perhaps more likely, that our calculated diffusion coefficient $D^{eff}_{H_2}$ or the calculated solubility S_{H_2} are slightly lower than the real values, thereby leading the model to underestimate the crossover at zero current density. In terms of pressure dependency, the data suggests that hydrogen transport to the gas phase is slightly inhibited by increased cathode pressure.

Crossover models with parameterized transfer coefficients corresponding to the hydrogen transport at the cathode have been fitted to experimental data before. Trinke et al. [17] report a value of 0.003 m s^{-1}, i.e., around one order of magnitude smaller than those depicted in Fig. 5. This agrees with the steep slope of crossover flux with respect to current density measured in [17]. Trinke et al. [30] determined transfer coefficients for various cathode CL ionomer contents (compare Section 4.2) obtaining transfer coefficients between 0.005 and 0.11 m s^{-1}. Omrani and Shabani [21] fitted $k^{cathode}_{H_2} = \alpha_k \cdot i^{\beta_k}$ as a function of current density for various literature data. Values on the order of 10^{-3} m s^{-1} to 10^{-2} m s^{-1} were obtained for practical current densities. The parameter β was determined to be between 0.1 and 0.8, i.e., $k^{cathode}_{H_2}$ was found to be almost constant or to increase with current density.

While most literature data produces qualitatively similar curves, some of the measured crossover data cannot be explained by the given transport model. For instance, Bernt et al. [7] measured a smaller crossover flux for a current density of 1 A cm^{-2} than for near-zero current density in Nafion^{TM} 212 membranes for pressures of 10–30 bar. These curves lead to unphysical values of $k^{cathode}_{H_2}$ as calculated with the model described here.

4. Cell influences on crossover

In addition to the operational influences which are included in the model presented in Section 2 such as current density, temperature, and cathode pressure, further influences on hydrogen crossover have been identified that are related to the materials and construction of the cell. Multiple works have shown cell compression to affect crossover, which will be discussed in Section 4.1. Further, the cathode material as well as the membrane itself can significantly impact crossover, as discussed in Sections 4.2 and 4.3, respectively.

4.1. Cell compression

The mechanical compression of the cell components in the direction into the cell plane has been shown to significantly affect hydrogen crossover [21,36,37].

Stähler et al. [36] investigated the effect of PTL compression on hydrogen crossover and cell voltage. They define the *compression value K* as the difference between the thickness of the relaxed cathode PTL and the actual PTL thickness in the cell. For a 200 µm carbon PTL, compression values K from 25 to 90 µm were investigated.

While an increase from $K = 25$ µm to $K = 50$ µm led to a significant voltage decrease due to lowered contact resistances, the improvement of the polarization behavior from any further compression was slight to insignificant. The crossover at very low current densities was independent of the cell compression, whereas increased compression was strongly associated with increased crossover at high current densities. This suggests that excessive cell compression exacerbates transport limitations. In fact, at a current density of $i = 3.5$ A cm^{-2}, the hydrogen

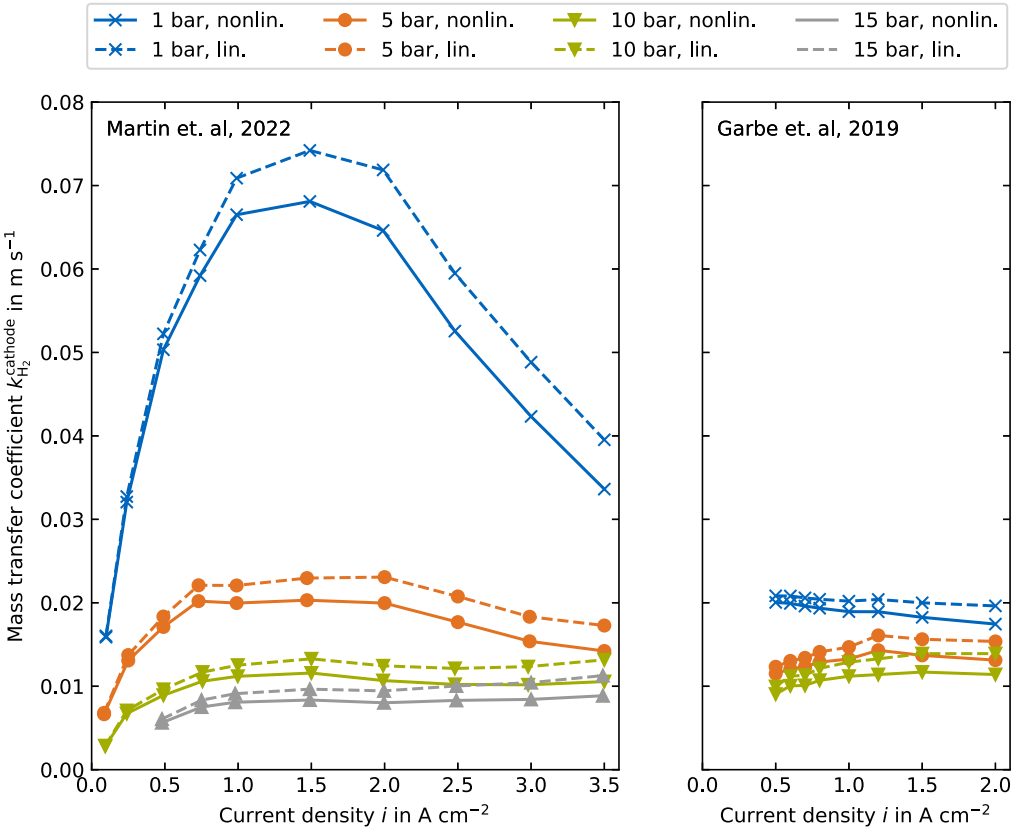

Fig. 5. Calculated mass transfer coefficient $k_{H_2}^{cathode}$ for data from Martin et al. [37] (left) and Garbe et al. [48] (right).

crossover flux and with it the hydrogen concentration in oxygen was more than six times as high at $K = 90\,\mu m$ than with $K = 25\,\mu m$.

Omrani and Shabani [21] were able to reproduce the crossover data measured by Stähler et al. [36] by assuming hydrogen transport away from the reaction site according to Eqs. (9) and (10) and fitting a current density dependent transfer coefficient $k_{H_2}^{cathode}$ to the experimental data. In addition to the mass transfer coefficient, a correlation of membrane temperature and current density was fitted, capturing possible heat transport limitations. The fitted mass transfer coefficients differ by a factor of roughly six at a current density of $i = 3$ A cm^{-2}. Further, the heat transport limitation was identified as another significant influence on crossover flux.

Martin et al. [37] measured the hydrogen crossover for compression values of 10–85 µm (uncompressed PTL thickness: 200 µm). As the cathode PTL is the most compressible element in the cell, its compression was assumed to be equal to overall cell compression. A two-dimensional measurement of contact pressure over the cell area was conducted, showing that high contact pressure is concentrated almost exclusively on the lands of the flow fields. The measured effect of cell compression on polarization and crossover behavior was qualitatively similar to that measured by Stähler et al. [36]. Again, increased cell compression slightly reduced the cell voltage but led to increased crossover at high current densities. Compared to Stähler et al. [36], the latter effect was less pronounced yet still significant at an almost three-fold increase of hydrogen crossover flux at a current density of $i = 3.5$ A cm^{-2}.

4.2. Cathode ionomer content

The cathode CL is a porous layer typically composed of a platinum (Pt)-containing catalyst, e.g., Pt supported on carbon, and an ionomer-containing binder. It has a wide variety of functions including the transport of electrons and protons to the reaction sites and the transport of hydrogen away from the reaction site to the gas phase. Its composition is often characterized by the ionomer content or the ionomer to carbon (I/C) ratio. While an increased ionomer content improves the mechanical stability and the ion conductivity of the layer, it generally reduces the electronic conductivity and obstructs mass transport of hydrogen out of the CL [4]. Accordingly, there is a trade-off between ionic transport and mass and electron transport.

Bernt and Gasteiger [50] experimentally confirmed this trade-off. The authors varied the anode CL ionomer content between 2.2 and 28 wt%, finding an optimum at 11.6 wt% ionomer content. Above this value, the voltage increased due to an increasing mass transport overvoltage and electronic isolation of the anode from the corresponding PTL. Below this value, the ionic transport was increasingly limited.

Bernt et al. [7] compared the hydrogen crossover flux and its dependency on current density in cells with cathode CL I/C ratios of 0.6, 0.9, and 1.2. Indeed, an increased slope of crossover flux with current density was measured for higher I/C ratios, pointing towards the postulated mass transport limitation of hydrogen at the cathode.

Trinke et al. [30] also varied the ionomer content of the cathode CL and measured the hydrogen crossover. They subsequently calculated the cathode CL transfer coefficient $k_H^{cathodeCL}$ assuming the linear transport model according to Eq. (32). Increasing the ionomer content between 10 and 40 wt.% led to a more than 20-fold increase of the calculated mass transfer coefficient of hydrogen from the cathode CL to the cathode PTL. Similar to Bernt and Gasteiger [50], Trinke et al. [30] found that intermediate ionomer content cathode CL ionomer contents around 30 wt.% produced the lowest cell voltage.

Overall, the cathode CL ionomer content has been shown to strongly affect hydrogen crossover, especially at high current densities. This

offers one possible explanation for the relatively wide spread of slopes of the crossover as a function of current density as shown in Fig. 3.

4.3. Membrane material

While the transport mechanisms are qualitatively the same for all membrane materials, material parameters can differ with membrane compositions. Briguglio et al. [51] measured hydrogen crossover to compare PEM electrolysis cells using $\delta^*_{mem} = 90\,\mu m$ Aquivion® membranes with and without a recombination layer. In contrast to typical Nafion™ membranes that are based on long side chain PFSA and typically exhibit an EW of 1100 g mol^{-1}_{eq}, commercial Aquivion® membranes for water electrolysis are based on short side chain PFSA and have an EW of 980 g mol^{-1}_{eq} [12]. Trinke et al. [17,27] examined Fumatech membranes with an EW of 910 g mol^{-1}_{eq}. The crossover measurements without recombination catalyst from Trinke et al. [17] and Briguglio et al. [12] are plotted in Fig. 6 and compared to those represented in Fig. 3 (also without recombination catalyst). Fig. 6 shows the data series from [17] in orange and that from [51] in blue. The marker symbols match the black symbols near the y-axis. These indicate the fitted crossover values at zero current density and $T = 60$ °C from Fig. 4.

The crossover data from [17] indicates increased diffusion in the investigated fumea EF-40 membranes compared to Nafion™. Regardless of the much higher slope of the crossover flux with the current density, the theoretical crossover at zero current density appears to be higher in these membranes than the reference values calculated for Nafion™ membranes. In contrast, Trinke et al. [27] found that the measured permeability of fumea EF-40 membranes (without electrical current) is lower than that of Nafion™ 117. One possible explanation is that the water content in the in situ experiments conducted in [17] was greater than the relatively low water content of $\lambda = 15$ used in the experiments in [27]. The greater slope in Fig. 6 may be partly caused by a hydrogen transport limitation from the cathode catalyst layer to the gas phase in the cathode channels. Therefore, it cannot necessarily be attributed to the membrane material.

The crossover towards zero current density in Aquivion® membranes, on the other hand, appears to indeed lie below that in Nafion™, as claimed by the manufacturer Solvay. The slopes of the two data series differ vastly with the 20 bar curve being notably concave and the 1 bar curve almost linear. Water drag, as described by Martin et al. [35], would qualitatively explain this. Zhang et al. [52] found lower crossover for Aquivion® compared to Nafion™ under fuel cell open circuit voltage conditions. Siracusano et al. [53] found similar crossover values between Nafion™ and Aquivion® in an electrolysis cell under operation.

Unfortunately, crossover data measured in non-Nafion™ membranes under varying operating conditions is relatively scarce in the literature, which makes a quantitative analysis of the differences between short and long side chain PFSA membranes in terms of crossover behavior difficult. As Fig. 6 points towards a significant effect of membrane composition on crossover behavior, we recommend more systematic research into crossover during electrolysis operation with different membrane materials. Reducing crossover and thereby enabling thinner membranes can be as effective for improving cell performance as improving ion conductivity.

Huang et al. [54] manufactured a PEEK-reinforced membrane based on PFSA and a hyperbranched polymer that was subsequently operated at a current density of up to 3 A cm^{-2} and up to 30 bar cathode pressure. The 90 μm thick sample outperformed Nafion™ 115 (125 μm) in terms of cell voltage and exhibited less than half the hydrogen crossover at a given set of conditions. Furthermore, excellent stability of the material was documented over 1200 h of operation at $i = 2$ A cm^{-2}. The authors ascribe the reduced crossover to the highly cross-linked polymer structure.

Fluorine-free hydrocarbon membranes pose a more radical pathway to higher-performing and more environmentally benign PEM electrolyzers [55,56]. For instance, Klose et al. [55] report approximately half the hydrogen permeability and approximately a third the Ohmic resistance in their 115 μm thick sulfonated poly(phenylene sulfone) based membrane compared to a slightly thinner Nafion™ 115 membrane. Ko et al. [56] report similar polarization curves of their approximately 50 μm thick membranes compared to Nafion™ 212, while their fluorine-free material exhibits a more than three-fold lower hydrogen permeability. Unfortunately, hydrocarbon membranes still lack mechanical stability and long-term stability in general for application in industrial PEM electrolyzers [55,57]. Mechanical stability may be improved in the mid-term by using fibrous reinforcements [56], blending, or co-polymerization [55].

5. Oxygen crossover

Oxygen crossover to the cathode is generally considered less detrimental to Faradaic efficiency and less critical in terms of safe operation than hydrogen crossover [33]. Due to the reaction stoichiometry, the oxygen in hydrogen is diluted twice as much as the hydrogen in oxygen. Further, most PEM electrolysis systems are operated at a differential pressure. The often near-atmospheric anode pressure results in a lower driving force for oxygen crossover compared to hydrogen. Finally, the Pt-based catalyst at the cathode catalyzes the recombination of oxygen and hydrogen to water. Therefore, only a fraction of the oxygen diffused through the membrane reaches the gas phase at the cathode side [33,58].

For these reasons, oxygen crossover to the cathode is much less studied than hydrogen crossover to the anode. On top of this, it is impossible to directly measure the actual oxygen flux through the membrane of a Pt-containing cell as most of it will recombine with hydrogen before leaving the cell. Nonetheless, oxygen crossover is an interesting phenomenon that has important implications.

Trinke et al. [33] measured oxygen crossover by using an electrolysis cell containing a Pt-free cathode catalyst. The measured oxygen crossover falls in the range of typical hydrogen crossover measured at 1 bar cathode pressure and 180 μm membrane thickness. The fact that one molecule of oxygen recombines with two molecules of hydrogen at the cathode could mean that oxygen crossover could be more detrimental to Faradaic efficiency than hydrogen crossover in case the anode pressure is similar to the cathode pressure.

Trinke et al. [33] argued that the oxygen transport phenomena are qualitatively the same as the ones for hydrogen as they measure the same characteristic increase of oxygen crossover with current density as has been observed for hydrogen. One notable asymmetry between hydrogen and oxygen crossover is that electroosmotic drag exacerbates oxygen crossover, while it partially mitigates hydrogen crossover. As a result, oxygen crossover may increase even more than linearly at increased current densities, although this has not been measured in practice.

Martin et al. [58] compared a series of Pt-free cathode catalysts in terms of their performance as a hydrogen evolution catalyst and in terms of the recombination taking place under electrolysis conditions. As expected, for the benchmark Pt/carbon (Pt/C) catalyst, the O_2 in H_2 fractions below 300 ppm were measured due to the high catalyst activity for the recombination reaction. This corresponds to a flux of approximately 0.025 mmol m^{-2} s^{-1} at a current density of 2 A m^{-2}. However, for Pt-free catalysts, an oxygen flux of up to 0.17 mmol m^{-2} s^{-1} was determined based on the oxygen still present in the hydrogen after possible partial recombination. For comparison, Martin et al. [35] reported a hydrogen flux of 0.2 mmol m^{-2} s^{-1} at the same current density and atmospheric cathode pressure.

The convex shape of the oxygen crossover over current density curves obtained by Martin et al. [58] could be caused by the kinetics of the recombination reaction or they could point towards the above

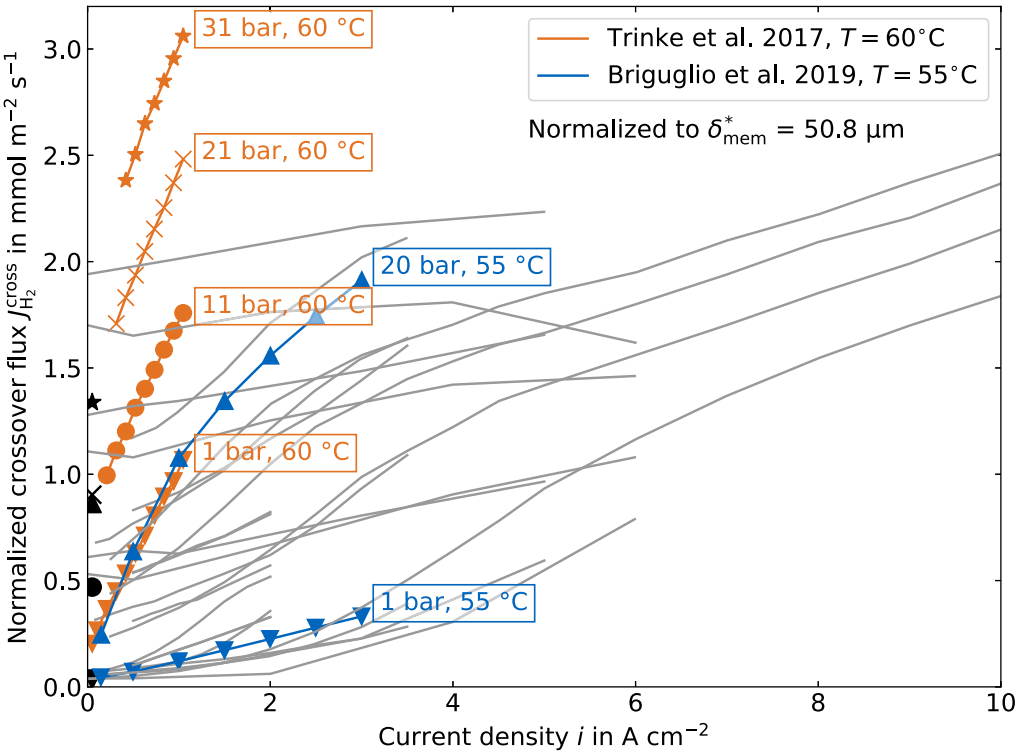

Fig. 6. Crossover flux data obtained with non-Nafion™ brand membranes taken from Briguglio et al. [51] and Trinke et al. [17] compared to data displayed in Fig. 3 (gray). The black symbols on the left show the theoretical crossover at zero current density found by interpolating literature data obtained with Nafion™ brand membranes for the respective conditions (see Section 3). (For interpretation of the references to color in this figure legend, the reader is referred to the web version of this article.)

described quadratic dependency of oxygen crossover on current density due to electroosmotic drag. On top of the recombination on the cathode CL, Martin et al. [58] found that a significant amount of recombination can take place on carbon PTLs as well. This must be kept in mind when estimating the losses caused by oxygen permeation.

In addition to negatively affecting the Faradaic efficiency, oxygen crossover is also involved in one of the major membrane degradation mechanisms in PEM electrolysis. Oxygen and hydrogen can combine on the cathode catalyst or Pt particles that have migrated into the membrane to form hydrogen peroxide [59–61]. The peroxide, in turn, can react via the Fenton reaction with metallic cations such as Fe^{3+} to form a hydroxide ion and a hydroxyl radical, which can attack the membrane [59–61]. Small amounts of Fe^{3+} impurities cannot be fully avoided in the water loop of industrial PEM electrolyzers. While it is widely accepted that oxygen crossover is involved in membrane degradation via this mechanism, it is difficult to prove that increased oxygen crossover causes degradation. On the contrary, Marocco et al. [60] measured approximately the five-fold fluoride release rate for Nafion™ 117 membranes compared to Nafion™ 212 membranes, although significantly more oxygen crossover is expected for the thinner Nafion™ 212 membrane. Kuhnert et al. [62] developed an accelerated stress test protocol that focuses on crossover-related membrane degradation by holding the cell at open circuit voltage while supplying hydrogen to the cathode and water and oxygen to the anode. Using a similar protocol with varying gas pressures would allow comparing similar cells that experience different crossover flux values for a substantial amount of time.

Further investigations of oxygen crossover and its implications are highly desirable. Oxygen crossover will be disproportionately exacerbated by the trend towards thinner membranes and increased current densities. While no direct implications on operational safety are expected, an increased crossover may affect the lifetime of the cathode [52] and the membrane and significantly reduce the Faradaic efficiency.

6. Recombination catalysts

In the last decade, there has been increased interest in introducing recombination catalysts within the electrochemical cell that allow to recombine hydrogen and oxygen inside the cell, thereby mitigating the safety issues associated with hydrogen crossover to the anode. Recombination catalysts are typically introduced as Pt-containing particles or layers between the cathode CL and the anode PTL. Fig. 7 and Table 4 give a comprehensive overview of investigated recombination strategies. These include membrane doting with relatively sparsely distributed Pt particles (Fig. 7D–G), additional catalyst layers laminated between two membrane elements (Fig. 7A–C), as well as the introduction of Pt in the anode CL (Fig. 7H–I).

Table 4 additionally gives an overview of the used recombination catalyst loading and whether or not a polarization curve and crossover data are available. Most works included a benchmark cell without recombination catalyst in their measurements and some conducted a durability test, although only two groups have tested cells for more than 1000 h.

While recombination catalysts do not mitigate the Faradaic losses caused by gas crossover, they enable the use of thinner membranes at the expense of lower Faradaic efficiency without violating any safety constraints. Since the overall efficiency is dominated by the voltage efficiency, but not the Faradaic efficiency, the energetic optimum would be to operate PEM electrolysis cells at extremely high crossover values with thin membranes [63]. While operating at maximum efficiency may not be realistic, recombination layers still enable operation closer to this optimum than would be possible otherwise.

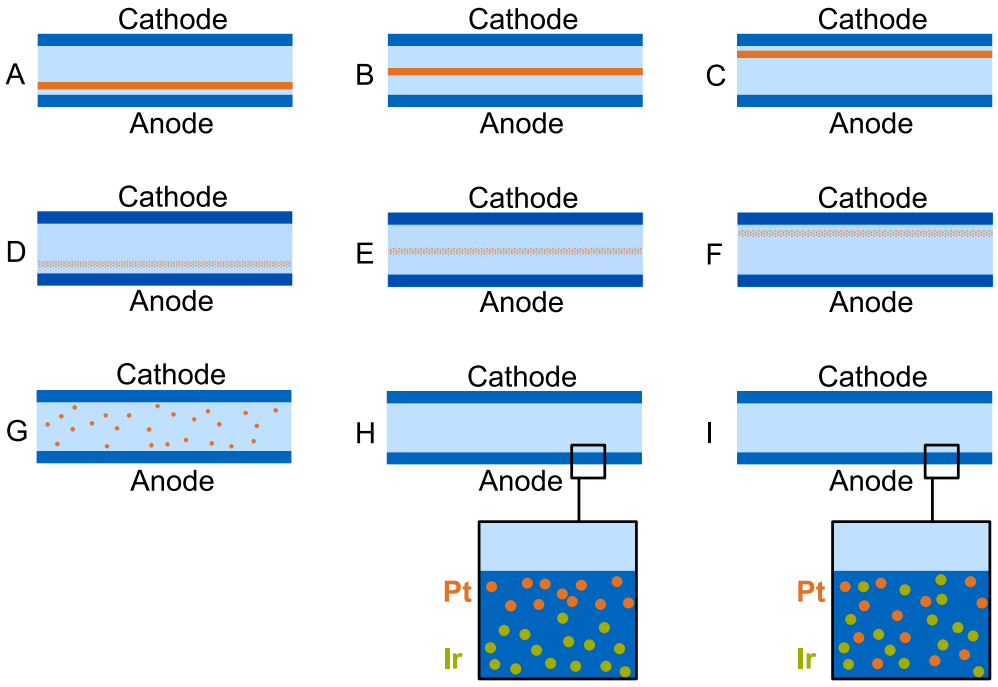

Fig. 7. Schematic representation of recombination layer positioning investigated in the literature [8,11,12,48,49,51,64–70]. A detailed allocation of the drawings to the references is given in Table 4.

Table 4
Overview of recombination layer concepts and main features of corresponding works.

Sketch (Fig. 7)	Short descriptions	Rec. cat. loading in mg_{Pt} cm^{-2}	Polarization curve	Crossover data	Benchmark w/o rec. cat.	Durability test	Source
A	Coated layer near anode	0.025	✓	✗	✓	3000 h	[64]
		Unknown	✗	✓	✓	5000 h	[65]
		0.04	✓	✓	✓	240 h	[66]
B	Coated layer near center	0.01–0.06	✓	✓	✓	✗	[8]
C	Coated layer near cathode	0.02	✓	✓	✓	245 h	[11]
D	Pt-doted layer near anode	0.01	✓	✓	✓	✗	[49]
		0.001–0.14	✓	✓	✓	✗	[68]
E	Pt-doted layer near center	0.01	✓	✓	✓	✗	[49]
F	Pt-doted layer near cathode	0.01	✓	✓	✓	✗	[49]
G	Pt-doted membrane	Unknown	✗	✓	✓	✗	[67]
		0.1	✓	✓	✓	✗	[48]
		0.01–0.06	✓	✓	✓	✗	[8]
		0.04	✓	✓	✓	100 h	[70]
H	Pt layer at anode	0.1 mg_{PtCo} cm^{-2}	✓	✓	✓	✗	[51]
		0.2	✓	✓	✗	✗	[12]
I	Pt mixed w/anode catalyst	0.2	✓	✓	✗	✗	[12]
		0.2 mg_{PtCo} cm^{-2}	✓	✗	✓	3500 h	[69]

Bessarabov [67] performed some of the first experiments regarding recombination layers for PEM electrolysis. A Pt-doped membrane was produced by the Takenaka–Torikai method that is based on contacting one side of a membrane with a reducing agent while the other side is in contact with a platinic acid solution ($PtCl_6^{2-}$). The resulting membrane contained hollow Pt particles mostly in proximity to the surfaces, which clearly showed activity for the recombination reaction. The recombination strategy falls into Fig. 7G. Garbe et al. [48] presented an improved method for Pt doping, wherein the steps of doping and the reduction of the Pt are separated in time. They obtained a membrane (type G in Fig. 7) with a highly uniform distribution of Pt particles, which allowed to keep the H_2 in O_2 fraction below 1% even at a current density of 0.5 A cm^{-2} and a cathode pressure of 10 bar without major additional overvoltage compared to the benchmark without the recombination catalyst. Garbe et al. [8] compared such a membrane to one similar to the one created by Bessarabov [67] at two different recombination catalyst loadings (0.01 and 0.06 mg_{Pt} cm^{-2}). There was a clear improvement for both membranes in terms of recombination when increasing the catalyst loading from 0.01 to 0.06 mg_{Pt} cm^{-2}. However, the membrane with the increased catalyst content towards the border exhibited a significantly higher resistance than that with the more even distribution.

As a further development of the method according to Fig. 7G, Zhang et al. [70] additionally included cerium–zirconium oxide particles in the membrane. As briefly described in Section 5, hydrogen peroxide can be generated by hydrogen and oxygen reacting on Pt. As this reaction is at least partly suppressed at the cathode potential, Pt that has migrated into the membrane may be primarily responsible for the deleterious effects of hydrogen peroxide and subsequent hydroxyl radical formation [59]. Therefore, there is reason to suspect increased degradation in the presence of a Pt-based recombination catalyst in the membrane. Zhang et al. [70] showed that Pt-doped membranes indeed

exhibit an increased fluoride release rate, and that cerium–zirconium oxide particles in the membrane can act as radical scavengers, limiting the fluoride release rate to levels below the baseline without any recombination catalyst. Good electrochemical performance was achieved, even with the Co-doped membrane. As tests were only performed over 100 h, more long-term tests would be desirable in the future to thoroughly separate initial effects from long-term behavior. Siracusano et al. [71] showed superior long-term stability of a Ce-impregnated Aquivion® membrane compared to reference samples in a 3500 h test. However, there was no recombination catalyst present in the MEA.

In addition to the different Pt-doped membranes, Garbe et al. [8] included a membrane according to Fig. 7B in their comparison. This membrane was manufactured by spray-coating of a half-thickness (Nafion™ 211 in this case) membrane with a catalyst ink based on Pt black and Nafion™ solution (loading 0.06 mg_{Pt} cm^{-2}) and hot-pressing it with another Nafion™ 211 membrane. Similar to the membrane with the relatively dense Pt distribution near the borders, this membrane exhibited good recombination characteristics, but an even higher overvoltage.

Similar approaches to Fig. 7B were also tested by Klose et al. [11] and Mirshekari et al. [64]. Klose et al. [11] included a spray-coated recombination layer near the cathode (Fig. 7C) by using two membranes of different thicknesses. Excellent recombination behavior and stability comparable to the reference cells over 250 h was shown. However, similar to Garbe et al. [8], a significant voltage increase due to the interlayer was measured at least in one sample.

Mirshekari et al. [64] constructed membrane electrode assemblies (MEAs) according to Fig. 7A and achieved an even lower voltage than their baseline cell despite lower electrode catalyst loadings and slightly increased overall membrane thickness. Moreover, the cells with recombination layers were operated for 3000 h at a current density of 1.8 A cm^{-2} exhibiting degradation rates of 24–37 μV h^{-1}. Ouimet et al. [65] produced a similar cell and showed stable operation for over 5000 h.

Martin et al. [49] proposed what can be thought of as a hybrid method between Pt-doped membranes and relatively dense interlayers by including a membrane layer with dispersed Pt nanoparticles at a desired position in the membrane. For this purpose, the entire membrane was spray-coated in layers, with some layers containing the Pt nanoparticles. With this approach, the authors were able to test the effect of the position of the interlayer, i.e., the performance difference between Fig. 7D, E, and F. They found that the closer the layer was towards the anode and the higher the anode pressure, the more effective was the recombination, pointing towards a limitation in oxygen availability for the recombination reaction. Similar to Garbe et al. [8,48], Martin et al. [49] found only a minor increase of the cell voltage due to the distributed Pt particles.

Based on the results by Martin et al. [49], Stähler et al. [66] considered only MEA type D, for which they suggested a more scalable production method based on slot-die coating. The production method produced repeatable results and the good polarization behavior and recombination from Martin et al. [49] were reproduced. Notably, membranes as thin as 20 μm were deployed, and the production method was demonstrated for areas up to 32.5 cm × 32.5 cm large MEAs. Abbas et al. [68] also considered MEA type D comparing different catalyst loadings. Catalyst loadings of 0.001, 0.007, 0.014, and 0.14 mg_{Pt} cm^{-2} were investigated, and diminishing returns in terms of recombination efficiency were found to set in around 0.007 mg_{Pt} cm^{-2}.

The approaches shown in Fig. 7H and I are different from the remaining ones in that the membrane itself remains unchanged and Pt is instead introduced into the anode CL. Briguglio et al. [51] introduced PtCo as a recombination catalyst between the anode CL and the membrane (according to Fig. 7H) after showing superior activity of PtCo compared to Pt black. Surprisingly, the cell with the recombination catalyst exhibited a better polarization behavior than the one without. However, the catalyst activity appeared to be too low to cope with the hydrogen crossover flux at a cathode pressure of 20 bar, for which only a fraction of the hydrogen recombined with oxygen. Briguglio et al. [12] compared this approach to the one where the recombination catalyst is mixed with the anode catalyst (see Fig. 7I). This approach yielded better performance in terms of recombination, but slightly lowered the cell's voltage efficiency. Finally, Pantò et al. [69] performed a 3500 h long-term test for the approach displayed in Fig. 7I. The degradation of the cell using the recombination catalyst was only 9 μV h^{-1} over the last 1000 h of the test.

One interesting aspect of recombination layers in general is that corporate research appears to be on a par if not ahead of academic research. In 2017, Johnson Matthey implemented, at least in experiments, thin membranes with recombination layers [72] that outperformed Nafion™ 117 in both crossover and resistance metrics. Furthermore, over the recent years, there has been considerable patent activity in the field [73–77].

Johnson Matthey [73] filed a patent on a MEA according to Fig. 7D using their own membranes. Plug power [74] filed a patent that appears to be most closely related to the MEA depicted in Fig. 7A, although it is generally difficult to distinguish between type A and type D in the patents. Gore [76] also filed a patent for a MEA according to Fig. 7A, although the focus here seems to lie on the two included reinforcement layers as well as the manufacturing of the MEA. Finally, Electric Hydrogen [75] filed a relatively general patent on a MEA using a recombination layer. Air Liquide [77] filed a patent in which a recombination catalyst is mixed into the anode catalyst as depicted in Fig. 7I.

While the mentioned patents by no means represent a comprehensive list, they do provide some insight into likely ongoing corporate research. For instance, radical scavengers such as ceria are mentioned in all four patents introducing Pt in the membrane itself [73–76]. Reinforcement layers were mentioned in three of the patents [73,75,76] and in an article on the activity of 3M in the field [13]. On the other hand membranes (type G) seem to be less considered for industrial application. Yang et al. [74] mention an increased Pt loading necessary with this strategy and it being challenging to realize in a roll-to-roll process as possible drawbacks.

While a considerable body of experimental works has been published in the past decade, there has been little focus on establishing suitable models to describe the kinetics and performance of recombination catalysts. Martin et al. [58] suggest a simple rate law for recombination on the cathode, which could be adapted for recombination layers. Ito et al. [78] modeled a reversible PEM fuel cell that includes Pt along with the Ir-based anode catalyst, similar to Fig. 7I. The recombination of permeated hydrogen with oxygen at the anode during electrolysis operation was modeled employing a simple ratio of hydrogen recombined to hydrogen permeated. Said ratio was determined to be between 0.7 and 1 for the considered experimental conditions.

7. Conclusion and future orientation

In this review, we reproduced and combined existing models in the domain of gas crossover. By fitting the resulting transport model to published experimental data, we showed a largely good agreement of measurements and mechanistic models of hydrogen crossover from previous literature. Particularly the diffusion part of the model, including the chosen correlations of diffusivity and solubility, was proven to be remarkably accurate by comparing its predictions to the experimental data extrapolated to zero current density. The combination of models and data paints a relatively clear picture of the transport mechanisms at play. These are primarily diffusion and supersaturation with possibly some additional effect of electroosmotic drag and differential pressure. Direct measurements of, e.g., the supersaturation or local temperature increase to ultimately confirm these mechanisms would be desirable but very difficult to achieve in practice. There is some remaining

uncertainty regarding the influence of differential pressure on drag and crossover but the majority of research points towards a negligible effect.

At high current densities, the hydrogen concentration at the cathode catalyst can be more than double the equilibrium concentration, i.e., the supersaturation can have more impact on diffusion than the cathode pressure (Fig. 2). Therefore, the cathode catalyst and transport layers strongly affects the crossover flux at high current densities. However, operation at low current densities is most critical for safety considerations. A these conditions, the membrane thickness and cathode pressure have the highest influence on crossover.

Crossover is linearly affected by the diffusion coefficient. However, based on Fig. 4, the uncertainty of the effective diffusion coefficient in Nafion^{TM} is low. As the operating temperature applied in industrial plants lies in a narrow range, Fig. 4 suggests a measurable but limited sensitivity of the temperature.

Oxygen crossover is much less studied than hydrogen crossover, partly due to lack of urgency as it does not cause any safety issues, partly due to the difficulty of directly measuring it. Possible recombination on the cathode PTL or even Pt-plated bipolar plates exacerbates this issue. Nonetheless, oxygen crossover has important implications for cell longevity and Faradaic efficiency, especially with ever-thinner membranes and higher current densities. At these conditions, the relative influence of supersaturation and electroosmotic drag compared to the one of the partial pressure (which will likely remain low for oxygen in the future) increases.

Due to the lack of experimental data, we did not fit any transport model for oxygen crossover. The same applies for non-Nafion^{TM} membranes, which, according to Fig. 6, may have significantly different diffusion properties. As the published data on alternative membrane materials points in a promising direction in terms of hydrogen permeability, we encourage more research around alternative membrane materials, including fluorine-free ones.

Various approaches for including recombination catalysts in PEM electrolysis cells have been tested, many of which show promising results. As the voltage efficiency dominates the overall efficiency, reducing the membrane thickness is one of the most impactful levers for improving overall electrolysis efficiency, even if it reduces the Faradaic efficiency. Recombination catalysts clear the path to very thin membranes by decoupling membrane thickness and hydrogen in oxygen fraction. This is especially true when used in conjunction with reinforcement layers, which decouple mechanical strength from membrane thickness to a certain degree.

On the downside, compensating crossover by employing recombination catalyst bears the risk of increased degradation due to the abundance of hydrogen and oxygen in the membrane material. Adequate long-term stability on the order of several years remains to be shown for cells including recombination layers. For example, ten years of continuous operation would likely require the degradation rate to be below 5 $\mu V\ h^{-1}$.

To our knowledge, there have not been any attempts to measure the effect of a recombination layer on Faradaic efficiency. On the one hand, by recombining the crossover gases inside the membrane, a steeper concentration gradient is expected to set in, potentially increasing product loss. On the other hand, without a recombination catalyst, oxygen may recombine at the cathode with hydrogen that otherwise would have ended up in the product stream, whereas with a recombination layer, crossover oxygen exclusively recombines with hydrogen that would have been lost by hydrogen crossover in any case. Measuring these effects would require accurate measurements of the gas flow rates and their compositions, which is challenging. However, a suitable setup could additionally provide new insights into oxygen crossover.

CRediT authorship contribution statement

Steffen Fahr: Conceptualization, Investigation, Methodology, Writing – original draft, Writing – review & editing. **Franziska K. Engel:** Investigation, Methodology, Writing – original draft, Writing – review & editing. **Sebastian Rehfeldt:** Funding acquisition, Supervision, Writing – review & editing. **Andreas Peschel:** Conceptualization, Supervision, Writing – review & editing. **Harald Klein:** Conceptualization, Funding acquisition, Supervision, Writing – review & editing.

Declaration of competing interest

The authors declare that they have no known competing financial interests or personal relationships that could have appeared to influence the work reported in this paper.

Acknowledgments

The authors gratefully acknowledge the financial support from the German Federal Ministry of Education and Research (BMBF) through H2Giga SINEWAVE (grant number 03HY123F).

Appendix A

Summary of equations

See Table A.1.

Table A.1
Summary of model equations as used in our models.

Equation	Validity
$J_{H_2}^{cross} = J_{H_2}^{diff} - J_{H_2}^{drag}$	Diffusion + drag
$J_{H_2}^{diff} = -D_{H_2}^{eff} \cdot \frac{d\, c_{H_2}}{d\, z}$	Fick diffusion
$D_i^{eff} = D_i \cdot \frac{\epsilon}{\tau}$	General
$D_i = D_{i0} \cdot \exp\left(\frac{-E_{A\,i}}{\bar{R} \cdot T}\right)$	10–60 °C [23]
$\epsilon = \frac{\lambda \cdot \bar{V}_{H_2O}}{\bar{V}_{mem} + \lambda \cdot \bar{V}_{H_2O}}$	General
$\bar{V}_{H_2O} = \frac{\bar{M}_{H_2O}}{\varrho_{H_2O}}$	General
$\bar{V}_{mem} = \frac{EW}{\varrho_{mem}}$	General
$J_{H_2}^{diff} = D_{H_2}^{eff} \cdot \frac{c_{H_2}^{cathode\ CL} - c_{H_2}^{anode\ CL}}{\delta_{mem}} \approx D_{H_2}^{eff} \cdot \frac{c_{H_2}^{cathode\ CL}}{\delta_{mem}}$	Diffusion only
$c_{H_2}^{cathode\ CL} = \frac{J_{H_2}^{transf\ cathode}}{k_{H_2}^{cathode}} + S_{H_2} \cdot p_{H_2}^{cathode}$	General
$J_{H_2}^{drag} = v_{H_2O} \cdot c_{H_2}$	General
$v_{H_2O} = \frac{n_{drag} \cdot i}{F \cdot c_{H_2O}}$	General
$n_{drag} = 0.0182\ K^{-1} \cdot T - 3$	30–70 °C [38]
$J_{H_2}^{transf\ cathode} = k_{H_2}^{cathode} \cdot \left(c_{H_2}^{cathode\ CL} - c_{H_2}^{cathode\ sat}\right)$	General
$J_{H_2}^{transf\ cathode} = \frac{i}{2F} - J_{H_2}^{cross} \approx \frac{i}{2F}$	Typical operation
$c_{H_2}^{cathode\ sat} = S_{H_2} \cdot p_{H_2}^{cathode}$	General
$S_i = 0.55\ \frac{mol}{m^3\ Pa} \cdot \exp\left(A_i + \frac{B_i}{T} + C_i \cdot \ln\left(\frac{T}{100\,K}\right)\right)$	273–353 K (H_2) [31], 273–348 K (O_2) [32]
$c_{H_2}(z) = \frac{J_{H_2}^{cross}}{v_{H_2O}} \cdot \left(e^{\left(\frac{v_{H_2O}}{D_{H_2}^{eff}}\right)\cdot(\delta_{mem}-z)} - 1\right)$	Diffusion + drag + Boundary conditions Eqs. (26)–(27)
$c_{H_2}(z) = \frac{J_{H_2}^{cross}}{D_{H_2}^{eff}} \cdot (\delta_{mem} - z)$	Diffusion only + Eqs. (26)–(27)

Nomenclature

Symbols and corresponding SI units

c	Molar concentration	mol m^{-3}
D	Diffusion coefficient	m^2 s^{-1}
E_A	Activation energy	J mol^{-1}
EW	Equivalent weight	kg $(mol\,SO_3H)^{-1}$
F	Faraday constant	A s mol^{-1}
J	Molar flux	mol m^{-2} s^{-1}
k	Mass transfer coefficient	m s^{-1}
$\bar{M}$	Molar mass	kg mol^{-1}
n_{drag}	Drag coefficient	–
P	Permeability	mol m^{-1} s^{-1} Pa^{-1}
p	Pressure	Pa
Δp	Pressure difference	Pa
$\bar{R}$	Universal gas constant	J mol^{-1} K^{-1}
S	Solubility	mol m^{-3} Pa^{-1}
T	Temperature	K
$\bar{V}$	Molar volume	m^3 mol^{-1}
z	Coordinate	m
δ_{mem}	Wet membrane thickness	m
δ^*_{mem}	Nominal membrane thickness	m
ϵ	Water volume fraction	–
λ	Water uptake	–
v	Velocity	m s^{-1}
τ	Tortuosity	–

Sub- and superscripts

avg	Average
diff	Diffusive
eff	Effective
H_2	Hydrogen
H_2O	Water
mem	Membrane
O_2	Oxygen
transf	Transfer

Abbreviations

AEL	Alkaline electrolysis
AEM	Anion exchange membrane
CL	Cathode layer
EW	Equivalent weight
PEM	Proton exchange membrane
PFSA	Perfluorosulfonic acid
PTL	Porous transport layer
SI	Supplementary information
SOEC	Solid oxide electrolysis cells

Appendix B. Supplementary data

Supplementary material related to this article can be found online at https://doi.org/10.1016/j.ijhydene.2024.04.248.

References

[1] Schmidt O, Gambhir A, Staffell I, Hawkes A, Nelson J, Few S. Future cost and performance of water electrolysis: An expert elicitation study. Int J Hydrogen Energy 2017;42(52):30470–92. http://dx.doi.org/10.1016/j.ijhydene.2017.10.045.

[2] Trattner A, Höglinger M, Macherhammer M-G, Sartory M. Renewable hydrogen: Modular concepts from production over storage to the consumer. Chem Ing Tech 2021;93(4):706–16. http://dx.doi.org/10.1002/cite.202000197.

[3] Bessarabov D, Millet P. Chapter 2: Brief historical background of water electrolysis. In: Bessarabov D, Millet P, editors. PEM water electrolysis vol 1. Elsevier; 2018, p. 17–42. http://dx.doi.org/10.1016/B978-0-12-811145-1.00002-2.

[4] Carmo M, Fritz DL, Mergel J, Stolten D. A comprehensive review on PEM water electrolysis. Int J Hydrogen Energy 2013;38(12):4901–34. http://dx.doi.org/10.1016/j.ijhydene.2013.01.151.

[5] Hemauer J, Rehfeldt S, Klein H, Peschel A. Performance and cost modelling taking into account the uncertainties and sensitivities of current and next-generation PEM water electrolysis technology. Int J Hydrogen Energy 2023. http://dx.doi.org/10.1016/j.ijhydene.2023.03.050.

[6] Kopp M, Coleman D, Stiller C, Scheffer K, Aichinger J, Scheppat B. Energiepark Mainz: Technical and economic analysis of the worldwide largest Power-to-Gas plant with PEM electrolysis. Int J Hydrogen Energy 2017;42(19):13311–20. http://dx.doi.org/10.1016/j.ijhydene.2016.12.145.

[7] Bernt M, Schröter J, Möckl M, Gasteiger HA. Analysis of gas permeation phenomena in a PEM water electrolyzer operated at high pressure and high current density. J Electrochem Soc 2020;167(12):124502. http://dx.doi.org/10.1149/1945-7111/abaa68.

[8] Garbe S, Samulesson E, Schmidt TJ, Gubler L. Comparison of Pt-doped membranes for gas crossover suppression in polymer electrolyte water electrolysis. J Electrochem Soc 2021;168(10):104502. http://dx.doi.org/10.1149/1945-7111/ac2925.

[9] Dang J, Zhang J, Deng X, Yang S, Liu B, Zhu X, Li Y, Yang F, Ouyang M. Hydrogen crossover measurement and durability assessment of high-pressure proton exchange membrane electrolyzer. J Power Sources 2023;563:232776. http://dx.doi.org/10.1016/j.jpowsour.2023.232776.

[10] Ayers K, Danilovic N, Harrison K, Xu H. PEM electrolysis, a forerunner for clean hydrogen. Electrochem Soc Interface 2021;30(4):67–72. http://dx.doi.org/10.1149/2.F16214IF.

[11] Klose C, Trinke P, Böhm T, Bensmann B, Vierrath S, Hanke-Rauschenbach R, Thiele S. Membrane interlayer with Pt recombination particles for reduction of the anodic hydrogen content in PEM water electrolysis. J Electrochem Soc 2018;165(16):F1271–7. http://dx.doi.org/10.1149/2.1241814jes.

[12] Briguglio N, Pantò F, Siracusano S, Aricò AS. Enhanced performance of a PtCo recombination catalyst for reducing the H2 concentration in the O2 stream of a PEM electrolysis cell in the presence of a thin membrane and a high differential pressure. Electrochim Acta 2020;344:136153. http://dx.doi.org/10.1016/j.electacta.2020.136153.

[13] Lewinski K. 3M NSTF for PEM water electrolysis. In: PEM electrolysis for hydrogen production. Principles and applications. Boca Raton, USA: CRC Press; 2016.

[14] Bessarabov D, Millet P. Chapter 5: Gas permeation in PEM water electrolyzers. In: Bessarabov D, Millet P, editors. PEM water electrolysis vol 1. Elsevier; 2018, p. 117–58. http://dx.doi.org/10.1016/B978-0-12-811145-1.00006-X.

[15] Schalenbach M, Carmo M, Fritz DL, Mergel J, Stolten D. Pressurized PEM water electrolysis: Efficiency and gas crossover. Int J Hydrogen Energy 2013;38(35):14921–33. http://dx.doi.org/10.1016/j.ijhydene.2013.09.013.

[16] Oberlin R, Stucki S, Christen H. Gas permeation through an SPE membrane during electrolysis. 33rd ISE-Meeting. Lyon, France; 1982.

[17] Trinke P, Bensmann B, Hanke-Rauschenbach R. Current density effect on hydrogen permeation in PEM water electrolyzers. Int J Hydrogen Energy 2017;42(21):14355–66. http://dx.doi.org/10.1016/j.ijhydene.2017.03.231.

[18] Afshari E, Khodabakhsh S, Jahantigh N, Toghyani S. Performance assessment of gas crossover phenomenon and water transport mechanism in high pressure PEM electrolyzer. Int J Hydrogen Energy 2021;46(19):11029–40. http://dx.doi.org/10.1016/j.ijhydene.2020.10.180.

[19] Dang J, Yang F, Li Y, Zhao Y, Ouyang M, Hu S. Experiments and microsimulation of high-pressure single-cell PEM electrolyzer. Appl Energy 2022;321:119351. http://dx.doi.org/10.1016/j.apenergy.2022.119351.

[20] Schalenbach M, Hoefner T, Paciok P, Carmo M, Lueke W, Stolten D. Gas permeation through Nafion. Part 1: Measurements. J Phys Chem C 2015;119(45):25145–55. http://dx.doi.org/10.1021/acs.jpcc.5b04155.

[21] Omrani R, Shabani B. Hydrogen crossover in proton exchange membrane electrolysers: The effect of current density, pressure, temperature, and compression. Electrochim Acta 2021;377:138085. http://dx.doi.org/10.1016/j.electacta.2021.138085.

[22] Franz T, Papakonstantinou G, Sundmacher K. Transient hydrogen crossover in dynamically operated PEM water electrolysis cells - A model-based analysis. J Power Sources 2023;559:232582. http://dx.doi.org/10.1016/j.jpowsour.2022.232582.

[23] Ito H, Maeda T, Nakano A, Takenaka H. Properties of Nafion membranes under PEM water electrolysis conditions. Int J Hydrogen Energy 2011;36(17):10527–40. http://dx.doi.org/10.1016/j.ijhydene.2011.05.127.

[24] Wise D, Houghton G. The diffusion coefficients of ten slightly soluble gases in water at 10-60° C. Chem Eng Sci 1966;(21):999–1010. http://dx.doi.org/10.1016/0009-2509(66)85096-0.

[25] Thampan T, Malhotra S, Tang H, Datta R. Modeling of conductive transport in proton-exchange membranes for fuel cells. J Electrochem Soc 2000;147(9):3242. http://dx.doi.org/10.1149/1.1393890.

[26] Fimrite J, Carnes B, Struchtrup H, Djilali N. Transport phenomena in polymer electrolyte membranes. J Electrochem Soc 2005;152(9):A1815. http://dx.doi.org/10.1149/1.1952647.

[27] Trinke P, Bensmann B, Reichstein S, Hanke-Rauschenbach R, Sundmacher K. Hydrogen permeation in PEM electrolyzer cells operated at asymmetric pressure conditions. J Electrochem Soc 2016;163(11):F3164–70. http://dx.doi.org/10.1149/2.0221611jes.

[28] Weber AZ, Newman J. Transport in polymer-electrolyte membranes. J Electrochem Soc 2004;151(2):A311. http://dx.doi.org/10.1149/1.1639157.
[29] Büchi FN, Scherer GG. Investigation of the transversal water profile in Nafion membranes in polymer electrolyte fuel cells. J Electrochem Soc 2001;148(3):A183. http://dx.doi.org/10.1149/1.1345868.
[30] Trinke P, Keeley GP, Carmo M, Bensmann B, Hanke-Rauschenbach R. Elucidating the effect of mass transport resistances on hydrogen crossover and cell performance in PEM water electrolyzers by varying the cathode ionomer content. J Electrochem Soc 2019;166(8):F465–71. http://dx.doi.org/10.1149/2.0171908jes.
[31] Young CL. Solubility data series: Hydrogen and deuterium. 1981.
[32] Battino R. Solubility data series: Oxygen and ozone. 1981.
[33] Trinke P, Bensmann B, Hanke-Rauschenbach R. Experimental evidence of increasing oxygen crossover with increasing current density during PEM water electrolysis. Electrochem Commun 2017;82:98–102. http://dx.doi.org/10.1016/j.elecom.2017.07.018.
[34] Trinke P. Experimental and model-based investigations on gas crossover in polymer electrolyte membrane water electrolyzers (Ph.D. thesis), Hannover: Gottfried Wilhelm Leibniz Universitat; 2020.
[35] Martin A, Trinke P, Bensmann B, Hanke-Rauschenbach R. Hydrogen crossover in PEM water electrolysis at current densities up to 10 A cm^{-2}. J Electrochem Soc 2022;169(9):094507. http://dx.doi.org/10.1149/1945-7111/ac908c.
[36] Stähler M, Stähler A, Scheepers F, Carmo M, Lehnert W, Stolten D. Impact of porous transport layer compression on hydrogen permeation in PEM water electrolysis. Int J Hydrogen Energy 2020;45(7):4008–14. http://dx.doi.org/10.1016/j.ijhydene.2019.12.016.
[37] Martin A, Trinke P, Stähler M, Stähler A, Scheepers F, Bensmann B, Carmo M, Lehnert W, Hanke-Rauschenbach R. The effect of cell compression and cathode pressure on hydrogen crossover in PEM water electrolysis. J Electrochem Soc 2022;169(1):014502. http://dx.doi.org/10.1149/1945-7111/ac4459.
[38] Suermann M, Pătru A, Schmidt TJ, Büchi FN. High pressure polymer electrolyte water electrolysis: Test bench development and electrochemical analysis. Int J Hydrogen Energy 2017;42(17):12076–86. http://dx.doi.org/10.1016/j.ijhydene.2017.01.224.
[39] Onda K, Murakami T, Hikosaka T, Kobayashi M, Notu R, Ito K. Performance analysis of polymer-electrolyte water electrolysis cell at a small-unit test cell and performance prediction of large stacked cell. J Electrochem Soc 2002;149(8):A1069. http://dx.doi.org/10.1149/1.1492287.
[40] Medina P, Santarelli M. Analysis of water transport in a high pressure PEM electrolyzer. Int J Hydrogen Energy 2010;35(11):5173–86. http://dx.doi.org/10.1016/j.ijhydene.2010.02.130.
[41] Hancke R, Bujlo P, Holm T, Ulleberg Øystein. High-pressure PEM water electrolyser performance up to 180 bar differential pressure. J Power Sources 2024;601:234271. http://dx.doi.org/10.1016/j.jpowsour.2024.234271.
[42] Friedrichs-Schucht M, Hasché F, Oezaslan M. Temperature dependence of water crossover in proton exchange membrane water electrolysis. ECS Trans 2023;111(4):3–11. http://dx.doi.org/10.1149/11104.0003ecst.
[43] Zawodzinski TA, Derouin C, Radzinski S, Sherman RJ, van Smith T, Springer TE, Gottesfeld S. Water uptake by and transport through Nafion® 117 membranes. J Electrochem Soc 1993;140(4):1041–7. http://dx.doi.org/10.1149/1.2056194.
[44] Luo Z, Chang Z, Zhang Y, Liu Z, Li J. Electro-osmotic drag coefficient and proton conductivity in Nafion® membrane for PEMFC. Int J Hydrogen Energy 2010;35(7):3120–4. http://dx.doi.org/10.1016/j.ijhydene.2009.09.013, URL: https://www.sciencedirect.com/science/article/pii/S0360319909013846.
[45] Kalinnikov A, Grigoriev S, Bessarabov D, Bouzek K. Two-phase mass transfer in porous transport layers of the electrolysis cell based on a polymer electrolyte membrane: Analysis of the limitations. Electrochim Acta 2021;387:138541. http://dx.doi.org/10.1016/j.electacta.2021.138541.
[46] Trinke P, Haug P, Brauns J, Bensmann B, Hanke-Rauschenbach R, Turek T. Hydrogen crossover in PEM and alkaline water electrolysis: Mechanisms, direct comparison and mitigation strategies. J Electrochem Soc 2018;165(7):F502–13. http://dx.doi.org/10.1149/2.0541807jes.
[47] Evans CE, Noble RD, Nazeri-Thompson S, Nazeri B, Koval CA. Role of conditioning on water uptake and hydraulic permeability of Nafion® membranes. J Membr Sci 2006;279(1–2):521–8. http://dx.doi.org/10.1016/j.memsci.2005.12.046.
[48] Garbe S, Babic U, Nilsson E, Schmidt TJ, Gubler L. Communication—Pt-doped thin membranes for gas crossover suppression in polymer electrolyte water electrolysis. J Electrochem Soc 2019;166(13):F873–5. http://dx.doi.org/10.1149/2.0111913jes.
[49] Martin A, Abbas D, Trinke P, Böhm T, Bierling M, Bensmann B, Thiele S, Hanke-Rauschenbach R. Communication—Proving the importance of Pt-interlayer position in PEMWE membranes for the effective reduction of the anodic hydrogen content. J Electrochem Soc 2021;168(9):094509. http://dx.doi.org/10.1149/1945-7111/ac275b.
[50] Bernt M, Gasteiger HA. Influence of ionomer content in IrO2 /TiO2 electrodes on PEM water electrolyzer performance. J Electrochem Soc 2016;163(11):F3179–89. http://dx.doi.org/10.1149/2.0231611jes.
[51] Briguglio N, Siracusano S, Bonura G, Sebastián D, Aricò AS. Flammability reduction in a pressurised water electrolyser based on a thin polymer electrolyte membrane through a Pt-alloy catalytic approach. Appl Catal B 2019;246:254–65. http://dx.doi.org/10.1016/j.apcatb.2018.12.079.
[52] Zhang H, Li J, Tang H, Lin Y, Pan M. Hydrogen crossover through perfluorosulfonic acid membranes with variable side chains and its influence in fuel cell lifetime. Int J Hydrogen Energy 2014;39(28):15989–95. http://dx.doi.org/10.1016/j.ijhydene.2014.01.076.
[53] Siracusano S, Baglio V, Stassi A, Merlo L, Moukheiber E, Arico' AS. Performance analysis of short-side-chain Aquivion® perfluorosulfonic acid polymer for proton exchange membrane water electrolysis. J Membr Sci 2014;466:1–7. http://dx.doi.org/10.1016/j.memsci.2014.04.030.
[54] Huang H, Zeng X, Zhong Z, Fan J, Li H. Low hydrogen permeability and high durability proton exchange membrane with three-dimensional acid-base crosslink structure for water electrolysis. J Membr Sci 2024;694:122408. http://dx.doi.org/10.1016/j.memsci.2024.122408.
[55] Klose C, Saatkamp T, Münchinger A, Bohn L, Titvinidze G, Breitwieser M, Kreuer K-D, Vierrath S. All–hydrocarbon MEA for PEM water electrolysis combining low hydrogen crossover and high efficiency. Adv Energy Mater 2020;10(14). http://dx.doi.org/10.1002/aenm.201903995.
[56] Ko EJ, Lee E, Lee JY, Yu DM, Yoon SJ, Oh K-H, Hong YT, So S. Multi-block copolymer membranes consisting of sulfonated poly(p-phenylene) and naphthalene containing poly(arylene ether ketone) for proton exchange membrane water electrolysis. Polymers 2023;15(7). http://dx.doi.org/10.3390/polym15071748.
[57] Thomassen MS, Reksten AH, Barnett AO, Khoza T, Ayers K. Chapter 6 - PEM water electrolysis. In: Tom Smolinka, Jurgen Garche, editors. Electrochemical power sources: fundamentals, systems, and applications. Elsevier; 2022, p. 199–228. http://dx.doi.org/10.1016/B978-0-12-819424-9.00013-6.
[58] Martin A, Trinke P, van Pham C, Bühler M, Bierling M, Holzapfel PKR, Bensmann B, Thiele S, Hanke-Rauschenbach R. On the correlation between the oxygen in hydrogen content and the catalytic activity of cathode catalysts in PEM water electrolysis. J Electrochem Soc 2021. http://dx.doi.org/10.1149/1945-7111/ac38f6.
[59] Liu H, Coms FD, Zhang J, Gasteiger HA, LaConti AB. Chemical degradation: Correlations between electrolyzer and fuel cell findings. In: Büchi FN, Inaba M, Schmidt TJ, editors. Polymer electrolyte fuel cell durability. New York, NY: Springer; 2009, p. 71–118. http://dx.doi.org/10.1007/978-0-387-85536-3_5.
[60] Marocco P, Sundseth K, Aarhaug T, Lanzini A, Santarelli M, Barnett AO, Thomassen M. Online measurements of fluoride ions in proton exchange membrane water electrolysis through ion chromatography. J Power Sources 2021;483:229179. http://dx.doi.org/10.1016/j.jpowsour.2020.229179.
[61] Feng Q, Yuan X-Z, Liu G, Wei B, Zhang Z, Li H, Wang H. A review of proton exchange membrane water electrolysis on degradation mechanisms and mitigation strategies. J Power Sources 2017;366:33–55. http://dx.doi.org/10.1016/j.jpowsour.2017.09.006.
[62] Kuhnert E, Heidinger M, Sandu D, Hacker V, Bodner M. Analysis of PEM water electrolyzer failure due to induced hydrogen crossover in catalyst-coated PFSA membranes. Membranes 2023;13(3). http://dx.doi.org/10.3390/membranes13030348.
[63] Hancke R, Holm T, Ulleberg Ø. The case for high-pressure PEM water electrolysis. Energy Convers Manage 2022;261:115642. http://dx.doi.org/10.1016/j.enconman.2022.115642.
[64] Mirshekari G, Ouimet R, Zeng Z, Yu H, Bliznakov S, Bonville L, Niedzwiecki A, Capuano C, Ayers K, Maric R. High-performance and cost-effective membrane electrode assemblies for advanced proton exchange membrane water electrolyzers: Long-term durability assessment. Int J Hydrogen Energy 2021;46(2):1526–39. http://dx.doi.org/10.1016/j.ijhydene.2020.10.112.
[65] Ouimet RJ, Yu H, Mirshekari G, Zeng Z, Bonville LJ, Bliznakov S, Niedzwiecki A, Mani P, Capuano C, Ayers KE, Maric R. Development of recombination layers to reduce gas crossover for proton exchange membrane water electrolyzers by reactive spray deposition technology. In: ECS meeting abstracts MA2020-02. 2020, p. 2469. http://dx.doi.org/10.1149/ma2020-02382469mtgabs.
[66] Stähler A, Stähler M, Scheepers F, Lehnert W, Carmo M. Scalable implementation of recombination catalyst layers to mitigate gas crossover in PEM water electrolyzers. J Electrochem Soc 2022;169(3):034522. http://dx.doi.org/10.1149/1945-7111/ac5c9b.
[67] Bessarabov D. (Invited) membranes with recombination catalyst for hydrogen crossover reduction: Water electrolysis. ECS Trans 2018;85(11):17–25. http://dx.doi.org/10.1149/08511.0017ecst.
[68] Abbas D, Martin A, Trinke P, Bierling M, Bensmann B, Thiele S, Hanke-Rauschenbach R, Böhm T. Effect of recombination catalyst loading in PEMWE membranes on anodic hydrogen content reduction. J Electrochem Soc 2022;169(12):124514. http://dx.doi.org/10.1149/1945-7111/aca6a0.
[69] Pantò F, Siracusano S, Briguglio N, Aricò AS. Durability of a recombination catalyst-based membrane-electrode assembly for electrolysis operation at high current density. Appl Energy 2020;279:115809. http://dx.doi.org/10.1016/j.apenergy.2020.115809.
[70] Zhang Z, Han Z, Testino A, Gubler L. Platinum and cerium-zirconium oxide co-doped membrane for mitigated H2 crossover and ionomer degradation in PEWE. J Electrochem Soc 2022;169(10):104501. http://dx.doi.org/10.1149/1945-7111/ac94a3.
[71] Siracusano S, Giacobello F, Tonella S, Oldani C, Aricò AS. Ce-radical scavenger-based perfluorosulfonic acid aquivion® membrane for pressurised PEM electrolysers. Polymers 2023;15(19). http://dx.doi.org/10.3390/polym15193906, Cited by: 0; All Open Access, Gold Open Access, Green Open Access.

[72] Price E. Durability and degradation issues in PEM electrolysis cells and its components. Johns Matthey Technol Rev 2017;61(1):47–51. http://dx.doi.org/10.1595/205651317X693732.
[73] Ellis PR, Gonzalez Herrera M, Rigg KM, Zalatis C. Catalyst coated proton exchange membranes for hydrogen producing water electrolyzers. 2021, WO23052749A1.
[74] Yang F, Lei C, Griffith A, Stone R, Mittelsteadt C. Electrolyzer membrane electrode proton exchange membrane water assembly. 2022, US020220243339A1.
[75] Sajjad SD, Eaglesham D, Danilovic N. Methods, devices, and systems for mitigating hydrogen crossover within an electrochemical cell. 2023, WO23172626.
[76] Bartels J, Lui W, Agapov AL. Improved electrochemical membrane. 2022, WO2022264008A2.
[77] Do NTQ. Performing an electrolysis. 2023, US2023220567A1.
[78] Ito H, Miyazaki N, Ishida M, Nakano A. Cross-permeation and consumption of hydrogen during proton exchange membrane electrolysis. Int J Hydrogen Energy 2016;41(45):20439–46. http://dx.doi.org/10.1016/j.ijhydene.2016.08.119.